

Dynamic crystallization in magmas

SILVIO MOLLO^{1,2} and JULIA EVE HAMMER³

¹ *Department of Earth Sciences, Sapienza - University of Rome, P. le Aldo Moro 5, 00185 Roma, Italy*

² *Instituto Nazionale di Geofisica e Vulcanologia, Via di Vigna Murata 605, 00143 Roma, Italy, e-mail: silvio.mollo@ingv.it*

³ *Department of Geology and Geophysics, SOEST, University of Hawaii 96822, Honolulu, Hawaii, USA, e-mail: jhammer@hawaii.edu*

Undercooling and crystallization kinetics are recognized increasingly as important processes controlling the final textures and compositions of minerals as well as the physicochemical state of magmas during ascent and emplacement. Within a single volcanic unit, phenocrysts, microphenocrysts and microlites can span a wide range of compositions, develop complex zoning patterns, and show intricate textures testifying to crystallization far from equilibrium. These petrographic complexities are not associated necessarily with magma chamber processes such as mixing or mingling of distinctly different bulk compositions but, rather, may be caused by variable degrees of initial magma-undercooling and the evolution of undercooling through time. Heat-dissipation and decompression are the most effective driving forces of cooling and volatile loss that, in turn, exert a primary control on the solidification path of magma. Understanding these kinetic aspects over the temporal and spatial scales at which volcanic processes occur is therefore essential to interpret correctly the time-varying environmental conditions recorded in igneous minerals.

This contribution aims to summarize and integrate experimental studies pertaining to the crystallization of magmas along kinetic or time-dependent pathways, where solidification is driven by changes in temperature, pressure and volatile concentration. Fundamental concepts examined in the last decades include the effect of undercooling on crystal nucleation and growth as well as on the transition between interface- and diffusion-controlled crystal growth and mass transfer occurring after crystals stop growing. We summarize recent static and dynamic decompression and cooling experiments that explore the role of undercooling in syn-eruptive crystallization occurring as magmas ascend in volcanic conduits and are emplaced at the surface. The ultimate aim of such studies is to decode the textural and compositional information within crystalline phases to place quantitative constraints on the crustal transport, ascent and emplacement histories of erupted and intrusive magmas.

Magma crystallization under dynamic conditions will be assessed also through a comparative description of the disequilibrium features in minerals found in experimental and natural materials. A variety of departures from polyhedral growth, including morphologies indicating crystal surface instability, dendritic structures, sector zoning and growth twins are linked to the rate at which crystals grow. These have implications for the entrapment of melt inclusions and plausibility for interpreting the growth chronology of individual crystals. A simple “tree-ring” model, in which the oldest part of the crystal lies at the centre and the youngest at the rim, is not an appropriate description when growth is non-concentric. Further, deviation from chemical

equilibrium develops in response to kinetically controlled cation redistributions related to the partitioning of major and trace elements between rapidly growing crystal and melt. The incorporation into the crystal lattice of chemical components in non-stoichiometric or non-equilibrium proportions has important implications for the successful interpretation of the conditions under which magmas crystallize and for the development of new equilibrium models based on mineral compositional changes.

Finally, it is important to stress that the main purpose of this contribution is to ignite research exploring the causes and consequences of cooling and decompression-driven crystal growth kinetics in order to appreciate in full the evolutionary paths of volcanic rocks and interpret the textural and compositional characteristics of their mineral constituents.

1. Crystal nucleation, growth and undercooling in laboratory experiments

This section builds on previous summaries of crystal nucleation and growth in laboratory experiments (Hammer, 2008; Kirkpatrick, 1981) in order to examine insights from recent publications, beginning with the laboratory techniques that impose superheating and undercooling, and their influences on solidification. In order to facilitate comparison across the breadth of recent work, we summarize trends and correlations relating experimental variables (temperature, pressure, cooling and decompression rate) to the most commonly reported compositional (major and minor element) and textural characteristics (*e.g.* crystal number density and volume fraction). The reader is referred to the original publications for additional data.

1.1. The significance of undercooling

Nucleation conditions dictate overall rock texture; growth conditions control crystal morphology, whether melt inclusions are likely to be enclosed and isolated, and the spatial heterogeneity of major and minor elements within crystals. Whether growth conditions permit incorporation of elements from a melt according to equilibrium partitioning or reflect kinetics of melt transport and crystal–melt interface reaction is a distinction of fundamental importance to the interpretation of magmatic history from rocks, and one that is amenable to laboratory study and modern microanalysis. The need to understand the time-evolution of magma crystallinity and evolving mineral compositions in the context of magma movement through the Earth's crust motivates experiments in which temperature, pressure and fluid composition are varied. The concept of undercooling is central to making sense of the time evolution of crystal nucleation and growth within these experimental and natural samples. Undercooling is defined as the difference between the system temperature and the temperature at which a phase saturates in the given liquid (Kirkpatrick, 1981). The degree of undercooling decreases during crystallization because the phase-saturation temperature decreases as the liquid composition changes. Undercooling is used inclusively here to refer to the thermodynamic driving force associated with either a decrease in temperature or compositionally induced increase in a melt's liquidus temperature driven by decompression under H₂O-saturated conditions. In studies of decompression-driven crystallization (*e.g.* Hammer and Rutherford, 2002; Couch *et al.*, 2003; Waters *et al.*, 2015), the term 'effective undercooling' is used to distinguish the driving force induced

by compositional change from that of temperature change. However, in both cases, it is quantified by the difference between the phase-in and system temperatures. The difficulty in ascertaining the actual undercooling during an experiment is addressed in some studies by the ‘nominal undercooling’ (Faure *et al.*, 2003) which ignores compositional changes and refers to the difference between the phase-in temperature of the starting liquid and the quench temperature. The distinction is important; during a cooling experiment the nominal undercooling is fixed, while the actual undercooling declines.

This driving force is balanced against component mobility, typically taken to scale with liquid viscosity (Zhang, 2010; Vetere *et al.*, 2015), to control the rates at which crystals nucleate and grow. Small growth rates associated with low undercooling require exceptional methodologies to resolve, exemplified by the *in situ* observations of olivine growing inside plagioclase-hosted melt inclusions of Jambon *et al.* (1992), and are relatively scarce in recent literature. Determining the crystal-growth rate, nucleation rate and overall magma solidification rate at moderate to high undercooling is a task amenable to quench-based laboratory techniques and relevant to a wide variety of volcano-magmatic situations.

Although numerical values for the rates of nucleation and growth vary by mineral, system composition, temperature with respect to the liquidus (*e.g.* undercooling as well as ‘superheating’ above the phase-in temperature), dwell time and possibly other variables, several features of plagioclase nucleation and growth kinetics (Hammer and Rutherford, 2002), illustrated schematically in Fig. 1 for decompressing rhyolite melt, appear to be generally applicable. The positions of the nucleation and growth-curve maxima are phase and system specific. The overall variation in nucleation rate is several orders of magnitude, compared with a factor of only <3 for growth rate (Swanson, 1977; Kirkpatrick, 1981; Hammer and Rutherford, 2002). Thus, nucleation rate exerts the fundamental control on the spatial distribution of solid in a crystallizing system: a high initial nucleation rate produces a large number-density of small crystals, and low nucleation rate produces fewer, larger crystals. Secondly, the separation between the maxima of the nucleation and growth curves, with the nucleation maximum occurring at higher undercooling, increases the likelihood that initial crystallization proceeds in either a nucleation-dominated or growth-dominated regime, associated with higher or lower undercooling, respectively. The tendency is manifest in rapidly decompressed synthetic and natural materials as a characteristic ratio of crystal-number density, N_A , to volume fraction of crystals, ϕ . Large ratios are associated with rapid ascent rates and moderate-to-high eruption intensities, because undercooling increases progressively with time. Low ratios are associated with slower decompression and vulcanian-to-dome-forming eruption styles (Brugger and Hammer, 2010a). In their study of crystallization in synthetic CaO–Na₂O–Al₂O₃–SiO₂ hapltonalite melt (CNAS rhyolite) following variable degrees of rapid decompression, Mollard *et al.* (2012) observe a strong correlation between undercooling and the number density of feldspar.

Undercooling may decrease, increase or remain constant, depending on whether the degree of solidification at earlier points along the pressure (or temperature) path is

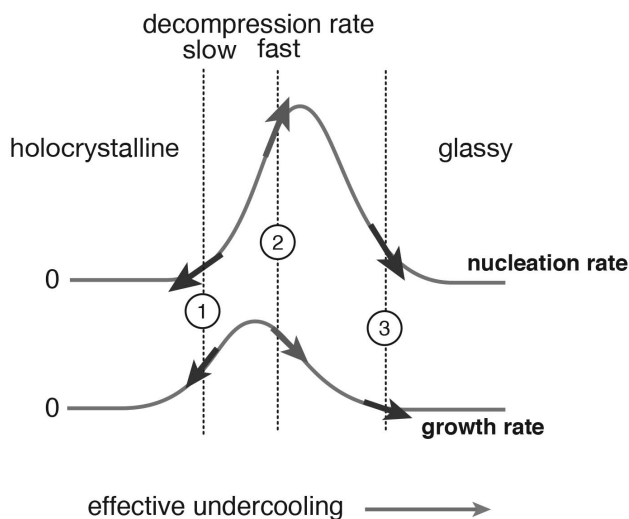


Figure 1. Schematic illustration of the functional dependence of crystal nucleation and growth rate on thermodynamic undercooling, based on classical theory (Tamman and Mehl, 1925; Dowty, 1980) and relevant experiments (e.g. Swanson, 1977; Hammer and Rutherford, 2002; Couch *et al.*, 2003). Three trajectories (among many possible) are highlighted. From a position of relatively low undercooling associated with slow magma decompression (or cooling), declining undercooling (arrows at 1) with time leads to coarsening of sparse crystals and holocrystalline texture. From a position of intermediate undercooling associated with low-intensity volcanic eruption, increasing undercooling (2) leads to a second nucleation event and phenocrystic texture. From a position of high initial undercooling, increasing undercooling (3) produces glassy texture.

sufficient to approach equilibrium, as summarized in Fig. 2. Intense volcanic eruptions that produce glassy pyroclasts are systems in which undercooling increases over the short time available for crystallization. Declining undercooling with time ultimately produces the coarse textures associated with intrusive rocks.

1.2. Assessing crystal nucleation in laboratory experiments

Actual nuclei of rock-forming minerals are too small for resolution by backscattered electron microscopy, and the refractory containers utilized in experimental techniques are typically opaque to *in situ* observation (with notable exceptions discussed below). Thus, the process of nucleation is typically approached indirectly, by assessing the number of crystals that grow to observable size ($\sim 1 \mu\text{m}$) in a given time following a perturbation from an initial crystal-poor or crystal-free state. Knowledge of the rate at which crystals form in response to an applied solidification-inducing thermodynamic driving force, which is typically cooling or decompression and referenced with respect to the liquidus temperature and H_2O -pressure ($P_{\text{H}_2\text{O}}$), thus constitutes a functional understanding of nucleation. Even by this modest definition of success, laboratory approaches to the study of nucleation in silicate melts involve challenges. Difficulties to be overcome include: (1) synthetic materials composed of oxide and carbonate

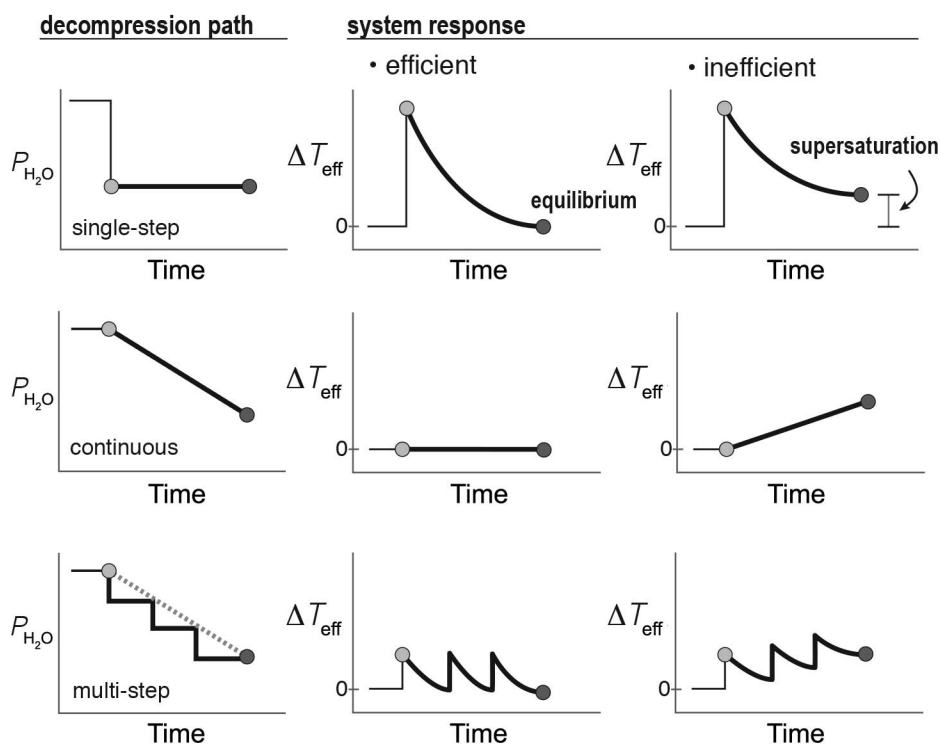


Figure 2. Relationships between experimental decompression paths and system response for instantaneous (single-step), continuous, and stepwise (multistep) changes in pressure. If change is imposed infinitesimally slowly, or at a rate at which solidification mechanisms (crystal nucleation and growth) are relatively rapid, the system maintains equilibrium and arrives at final pressure (P_f) at a state of zero undercooling. If the rate of solidification is unable to keep pace with pressure decrease, undercooling increases with time. Stepwise decompression produces spikes in undercooling and potentially different textures and phase compositions at P_f , despite similar time-integrated rates of change, because the rates of transformation differ along the path. Most of the decompression experiments described in this review represent the third scenario. This conceptual framework is also relevant to experiments in which temperature decrease drives solidification.

reagents must first react in order to become silicate melts; failure to homogenize the liquid could provide sites for heterogeneous nucleation that are difficult to characterize (Iezzi *et al.*, 2008; Vetere *et al.*, 2013, 2015); (2) natural starting materials must be crushed in order to load them into capsules, and the pores and grain interfaces that result from grinding natural glass and crystal-rich starting materials might provide energetically advantageous surfaces that are not present in nature (Vetere *et al.*, 2015); (3) the entire thermal history of the material, including run-up to initial conditions (Ni *et al.*, 2014) and superliquidus heat treatments (Sato, 1995; Pupier *et al.*, 2008; Waters *et al.*, 2015), may influence the distribution of subcritical clusters poised

to become nuclei; and (4) containers and exterior bead surfaces provide energetically favourable sites for heterogeneous nucleation of spinel-structured oxide phases (Berkebile and Dowty, 1982; Mollo *et al.*, 2012a), which can influence the formation of silicates through the formation of boundary layers or heterogeneous nucleation assisted by epitaxy (*e.g.* clinopyroxene on spinel-structured oxides; *cf.* Hammer *et al.*, 2010; Vetere *et al.*, 2015).

Noting that the time scale of structural relaxation, τ , in silicate melt is $<10^{-7}$ s, as estimated using reasonable values for η (viscosity of the melt) and G (shear modulus) by means of the Maxwell (Dingwell and Webb, 1990) relation,

$$\tau = \eta/G \quad (1)$$

Vetere *et al.* (2013) suggested that melt structure at the liquidus can be considered path-independent. They strive to eliminate extrinsic defects such as chemical and physical heterogeneities (*e.g.* bubbles or relict crystals) by preparing six starting materials for one-atmosphere cooling experiments as combinations of natural basalt ($T_l = 1230^\circ\text{C}$) and rhyolite ($T_l = 1045^\circ\text{C}$), repeatedly powdering and fusing the mixtures to 1600°C ($+\Delta T = 370\text{--}555^\circ\text{C}$) and annealing the homogenized glasses for 2 h at 1400°C ($+\Delta T = 170\text{--}355^\circ\text{C}$) before performing the cooling experiments, which begin after a 2 h dwell period at 1300°C ($+\Delta T = 70\text{--}255^\circ\text{C}$). The authors evaluate the success of this sequence for producing structurally relaxed liquids at 1300°C by demonstrating reproducibility of final crystal texture in duplicate runs and comparing the run products against similarly prepared and cooled samples that had undergone an extra 40 h dwell period at 1400°C ($+\Delta T = 170\text{--}355^\circ\text{C}$) prior to the dwell at 1300°C . The consistency of mineralogy, crystal shape and abundance in the two series demonstrates that the additional dwell at 1400°C had no effect, and this is interpreted as a consequence of having eliminated extrinsic defects in the previous steps. It is unknown what effect, if any, the cumulative superheating (16 h by $T > 370^\circ\text{C}$ imposed on all samples) had on nucleation, and whether a similar material would have nucleated crystals at a higher rate had it been held nearer the liquidus before cooling. That is, the experiments performed are not capable of evaluating the relevance of the Maxwell structural relaxation time in describing a system's readiness for nucleation. Are intrinsic artefacts introduced by superheating, even as extrinsic artefacts are eliminated?

If diffusive homogenization over the length scale of experimental charges provides the relevant time scale for the formation of the equilibrium, structurally-relaxed distribution of subcritical clusters (Dingwell, 1995; Vetere *et al.*, 2013), it should be possible to isolate the extrinsic and intrinsic effects and study homogeneous nucleation with a matrix of experiments with high- and low-temperature dwell periods of varying duration and superheating degree, that eliminate possible foreign substrates (assuming they are soluble in the melt), and subsequently erase intrinsic impediments to nucleation.

1.3. Crystal nucleation as a means of examining volcanic processes

The studies described in the previous section target the kinetics of crystal nucleation as an explicit goal and necessarily consider the degree and duration of superheating as

factors influencing subsequent crystallization. Other studies manipulate nucleation kinetics in order to achieve a particular texture in the run products. In their study of crystallization in H₂O-obsidians, rhyolite and dacite, Waters *et al.*, (2015) modulated the starting pressure in order to control nucleation of plagioclase during subsequent decompression. Decompression experiments initiated from 44 MPa above the plagioclase-in stability curve at the experimental temperature produce fewer, larger crystals in aphyric obsidian than those held 6 MPa below the plagioclase-in curve, even though the subliquidus dwell period (48 h) produced no discernable feldspar and the crystal volume fraction for a given final pressure was similar. This degree of superheating was a requirement for matching the texture of natural samples, perhaps because it reduced the number of sites available for immediate growth. A similar technique was employed by Lofgren *et al.* (2006), on the basis of earlier work (*e.g.* Lofgren and Lanier, 1992), in a dynamic cooling study of rare earth element partitioning in sector-zoned pyroxenes. The experiments were initiated <5°C above the liquidus temperature, with the goal of reducing, but not eliminating, the number of sites for immediate growth.

Given the importance of solidification kinetics (*via* control on nucleation and growth rates) on undercooling and the importance of crystallization in prior time increments in controlling undercooling (Fig. 2), the manner in which samples are decompressed would logically exert a fundamental control on final texture. Experiments in which undercooling is applied instantaneously are uniquely capable of resolving nucleation and growth rates as a function of driving force; incremental cooling or decompression allows investigation of crystallization in a manner more likely to occur in nature. Decompression experiments prior to 2009 were executed by bleeding in a series of small steps the gas or water exerting pressure on the capsules in the hydraulic line (Hammer and Rutherford, 2002; Couch *et al.*, 2003; Martel and Schmidt, 2003). Brugger and Hammer (2010a) used a specially designed automated screw-jack mechanism to impose decompression quasi-continuously on crystal-poor rhyodacite, and included two experiments in which the same integrated decompression rate (1 MPa h⁻¹) was achieved continuously and in steps of 10 MPa each. The multi-step decompression produced qualitatively different crystal texture and composition from the continuous decompression. In the multi-step runs, crystals are more skeletal, more inhomogeneously distributed, and lower in number density; all indications that nucleation was inhibited and growth occurred at relatively high undercooling. Evidently the higher driving force did not translate into more rapid crystallization, and the system strayed further from equilibrium during decompression (*e.g.* third scenario in Fig. 2). Nowak *et al.* (2011) introduced a valve capable of metering incremental gas in the IHPV setup. This device was used to study degassing kinetics and was employed in crystallization experiments of Fiege *et al.* (2015), although the results were not compared with multi-step style decompression. Preliminary experiments suggest that stepwise decompression produces similar plagioclase contents regardless of the number of steps (n , for n from 1 to 25), appreciably different plagioclase and pyroxene compositions if $n < 5$, and plagioclase morphology that is sensitive to $n \leq 25$ (Hammer *et al.*, unpublished data).

1.4. Cooling and decompression, imposed separately and together

Shea and Hammer (2013) address the question of whether decompression-driven crystallization produces a fingerprint distinct from cooling-driven crystallization by using pairs of single-step decompression (SSD) and single-step cooling (SSC) experiments (Fig. 3a). Dwell pressures in the SSD were selected to match effective undercooling values of 52, 82, 112, 137 and 155°C imposed by the corresponding dwell temperatures in the SSC series. Natural lava from the Mascota volcanic field, Mexico (previously characterized in phase equilibrium experiments by Moore and Carmichael, 1998) was crushed lightly prior to hydration and equilibration at initial conditions below the stability curves of plagioclase, clinopyroxene, olivine and Cr-spinel. The two series produced similar plagioclase abundances, similar nucleation and growth rates during dwell periods of 12, 24 and 48 h, and similar compositions up to relatively high undercooling ($\Delta T = 112^\circ\text{C}$, final pressure $P_f = 45$ MPa in the SSD series).

The insensitivity of outcome to solidification driving force at conduit temperatures and pressures could be useful in numerical modelling of magma crystallization paths. However, consistent differences emerge at even higher undercooling. Feldspar number density and abundance are higher in the decompression series, peaking at the largest undercooling examined (155°C). Because of more dissolved H₂O content throughout the cooling runs, amphibole and olivine are the dominant ferromagnesian phases; Ca-clinopyroxene dominates in the decompression runs. This mineralogical difference has an unexpected implication regarding feldspar texture. Conspicuous clustering of plagioclase crystals around clinopyroxene and correlated number densities of these phases suggest that clinopyroxene provides a substrate for heterogeneous nucleation of plagioclase. Vetere *et al.* (2015) report a similar result for cooling of nominally anhydrous basaltic liquids. Heterogeneous nucleation of feldspar on clinopyroxene is not recognized in silicic magma compositions, and could be an important factor controlling the formation and texture of feldspar in mafic-intermediate magmas.

Arzilli and Carroll (2013) studied crystallization of trachyte melt in response to a variety of supersaturation mechanisms, including isobaric cooling, isothermal decompression, and a combination of cooling and decompression using a natural obsidian from the Breccia Museo Member of the Campanian Ignimbrite, Campi Flegrei containing 10 vol.% crystals (alkali feldspar, clinopyroxene, magnetite and biotite). Initial conditions include a variety of temperature-pressure combinations above the feldspar stability curve, and consequently, a range in effective superheating from 15 to 131°C. The temperature drops and decompressions were performed rapidly and the charges quenched after 2–14 h dwell periods at static (isothermal, isobaric) conditions. Because superheating and undercooling are not isolated as experimental variables (Fig. 3b), it is uncertain whether differences in feldspar abundance in run products at the same final conditions are due to path through *P-T* space, H₂O content at initial conditions, magnitude of initial superheat, or possibly failure to achieve equilibrium at the initial conditions during the 2 h hydration period. However, feldspar textures in the run products indicate consistently that nucleation dominates crystallization at low pressure and temperature, whereas growth dominates at conditions closer to the

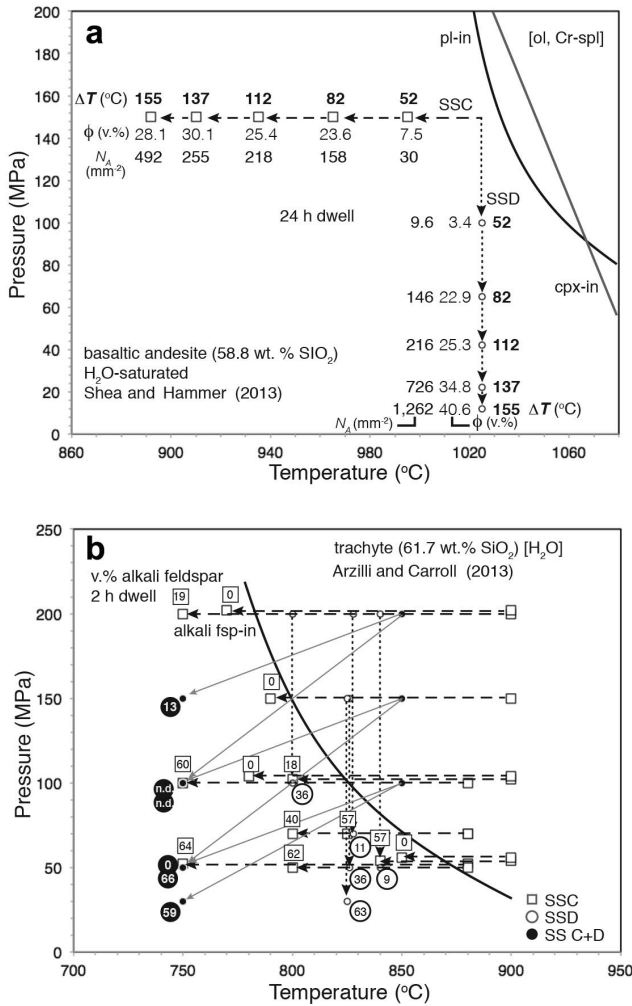


Figure 3. Pressure-temperature diagrams summarizing experiments on basaltic andesite and trachyte by Shea and Hammer (2013) and Arzilli and Carroll (2013), respectively. In (a), values of plagioclase feldspar abundance and number density are shown beside each set of final conditions. In (b), the mineral-in curves for biotite, titanomagnetite and clinopyroxene are omitted for clarity. All experimental conditions occur within the stability field of titanomagnetite, but only experiments above 100 MPa are within the biotite stability field, and experiments at high initial superheating begin outside of the clinopyroxene stability field and end within it. Experimental paths performed at the same pressure and temperature are separated slightly, for legibility. The values of alkali feldspar crystallized abundance in decompression-only experiments are indicated with open circles positioned to the lower right of the T_f , P_f coordinates; cooling experiment values are shown with squares above the T_f , P_f points, and decompression+cooling values are in shaded circles, positioned to the lower left of the T_f , P_f points. The two SSC experiments labelled 57 and 62 vol.% feldspar correspond to the path type and conditions producing a second nucleation burst at long dwell times (described in text).

feldspar stability curve. Moreover, the time series provide constraints on the changes in the rates of crystal growth, nucleation and crystallization rate (for fixed initial conditions and superheat) following identical perturbations in environmental conditions. Interestingly, although the nucleation rate decreases progressively during the dwell periods of the decompression runs, several of the longer-duration cooling-only runs undergo a second feldspar nucleation event. A difference in the time-evolution of effective undercooling (*e.g.* different versions of inefficient system response; Fig. 3a,b) may be correlated with supersaturation mechanism.

1.5. Novel apparatus

The vast majority of experimental studies involve sealing reactants inside (opaque) noble metal capsules capable of withstanding high temperatures and pressures, bringing the capsules to magmatic conditions inside a furnace and pressure vessel, rapidly cooling them to ambient conditions in an attempt to quench-in the magmatic state, and dissecting the run product to analyse the crystals. Schiavi *et al.* (2009) departed from this approach and achieved continuous *in situ* observation of magma crystallization by containing sample material in an externally heated moissanite cell at ambient pressure. Although temperature control is an issue with this methodology (Hammer, 2009), its strength is that continuous observation alleviates concern about quench effects and allows observation of crystal populations and individual crystals through time. Schiavi *et al.* (2009) observed growth of prismatic feldspar crystals in nominally dry synthetic high-K andesitic basalt (in which FeO was replaced by MnO for optical transmissivity) during 15–50 min dwell periods at 900°C, ~330°C below its liquidus, noting that coalescence is the dominant process of grain-size increase. When neighbouring crystals impinge, the result is continued growth of the coalesced units, whether or not the neighbours were aligned initially. Using an improved version of the apparatus, Ni *et al.* (2014) observe olivine and clinopyroxene crystals growing from initially superheated synthetic basalt along a variety of thermal paths involving continuous cooling as well as isothermal dwelling.

Because the systems examined with the *in situ* technique (Schiavi *et al.*, 2009; Ni *et al.*, 2014) crystallize far from equilibrium, and the degree of phase undercooling is not constrained, the geologic relevance of the plagioclase, olivine and clinopyroxene growth-rate values obtained ($2.3\text{--}4.8 \times 10^{-9} \text{ m s}^{-1}$, $2\text{--}7 \times 10^{-9} \text{ m s}^{-1}$ and $6\text{--}17 \times 10^{-9} \text{ m s}^{-1}$, respectively) is difficult to assess. Insights about growth processes, rather than absolute growth rate values, are the chief contributions of the *in situ* studies. Intriguing results from Ni *et al.* (2014) included: (1) melt-inclusion entrapment and closure in the absence of measurable thermal cycling; (2) size-proportionate growth (described earlier by Kile and Eberl, 2003), in which larger crystals grow faster than smaller crystals; (3) unchanging rate of crystal growth during cooling by 100°C, despite evolution from tabular to hopper crystal morphology; and (4) coarsening of the population by size-proportionate growth and dissolution of small crystals. The last observation is consistent with results from hydrous magma decompression experiments (*e.g.* Brugger and Hammer, 2010a; Mollard *et al.*, 2012; Arzilli and Carroll, 2013), and

has important implications for interpreting crystal-size distributions (CSDs). Because coarsening is typically associated with near-equilibrium conditions (Cabane *et al.*, 2005; Higgins and Roberge, 2003), a decrease in the frequency of crystals in the smallest size classes encountered by Brugger and Hammer (2010b) was interpreted as inadequate stereological correction of cut effects. The *in situ* observations suggest that reduction of crystal–melt interfacial energy among silicate phases is sufficient to drive redistribution of mass from small to larger crystals, even at conditions far from equilibrium.

2. Interface- vs. diffusion-controlled reactions

In igneous settings, the interpretation of rock textures and compositions is commonly based on the assumption of equilibrium between minerals and the host magmas. This general expectation justifies, most of the time, the use of thermodynamically derived formalisms to reconstruct the intensive variables of the plumbing systems, as well as to model the geochemical evolution of erupted magmas (*e.g.* Putirka, 2008 and references therein). During recent decades, however, a gamut of studies has reported clear evidence of disequilibrium features in both intrusive and effusive volcanic rocks on scales ranging from the hand specimen to the outcrop (*e.g.* DePaolo and Getty, 1996; Roselle *et al.*, 1997; Müller *et al.*, 2004; Nabelek, 2007; Baker, 2008). It has also documented that both the textural evolution and compositional change of minerals are not necessarily related to the attainment of equilibrium, but rather the development of reaction kinetics along most of the crystallization path of magma leading to final disequilibrium textures and compositions (Baker and Grove, 1985; Hammer, 2006, 2008; Iezzi *et al.*, 2008, 2011; Del Gaudio *et al.*, 2010; Mollo *et al.*, 2010, 2011a,b).

With respect to the superliquidus state of magma, a certain amount of undercooling is always necessary for the onset of crystal nucleation and growth. The degree of undercooling (ΔT) is the difference between the liquidus temperature (T_l) and the final resting temperature (T_r) of the system (Fig. 4a). Low-to-large ΔT can be achieved prior to crystallization in response to variable degassing and cooling paths experienced by magmas. Once crystal nucleation occurs, crystal growth may proceed with variable rates as a function of the magnitude of ΔT . For the simplest case represented by a diopsidic liquid (CaO·MgO·2SiO₂), the growth rate of clinopyroxene has been determined experimentally over the effect of increasing undercooling (Nascimento *et al.*, 2004 and references therein). The data span a range of about seven orders of magnitude with a variety of undercoolings between the glass transition temperature (T_g) and liquidus temperature of the diopsidic liquid (T_l) (Fig. 4b). As T_r approaches T_l , the crystal growth rate (G) increases to a maximum value (G_{\max}) corresponding to the shift of the crystal-growth regime from diffusion-controlled to interface-controlled (*e.g.* Dowty, 1980; Lofgren and Smith, 1980; Kirkpatrick, 1981; Hammer, 2008). Small undercoolings and high T_r (approaching T_l) promote interface-controlled crystal growth mechanisms where the diffusion of chemical elements in the melt prevails over the crystal growth rate.

Minerals develop euhedral textures (*e.g.* prismatic, tabular, well faced, *etc.*), core-to-rim crystal zoning is generally lacking and the composition of the melt next to the

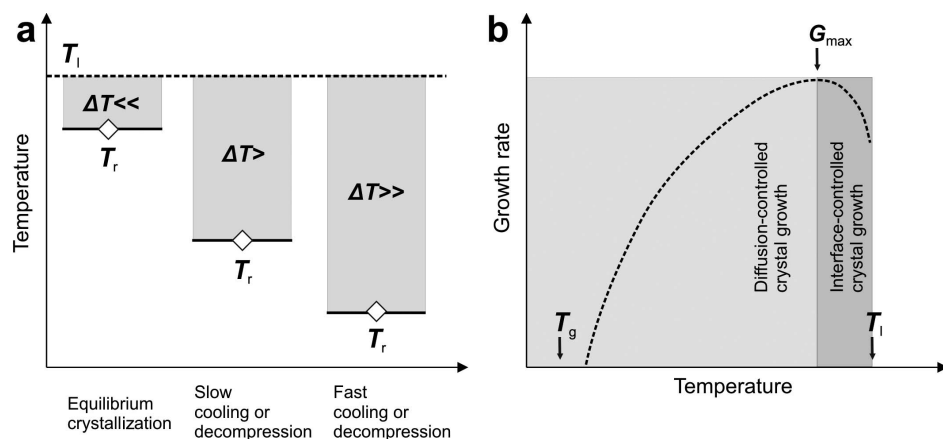


Figure 4. Equilibrium and dynamic crystallization of magma as a function of undercooling (a). The degree of undercooling (ΔT) is the difference between the liquidus temperature (T_l) and the final resting temperature (T_r) of the system. Small-to-large ΔT can be achieved prior to crystallization in response to variable degassing and cooling paths experienced by magmas. Schematic sketch showing the relationship between growth rate and undercooling for a diopsidic liquid derived by Nascimento *et al.* (2004) (b). The undercooling is confined between the glass transition temperature (T_g) and liquidus temperature of the melt (T_l). As T_r approaches T_l , the crystal growth rate (G) increases up to a maximum value (G_{max}) corresponding to the shift of the crystal-growth regime from diffusion-controlled to interface-controlled.

crystal surface is homogeneous (Fig. 5a). In contrast, large undercoolings and low T_r (approaching T_g) lead to diffusion-controlled crystal-growth processes where the crystal growth rate exceeds the ability of chemical elements to diffuse through the melt. The crystal texture is anhedral showing a wide spectrum of disequilibrium features (*e.g.* dendritic, skeletal, swallowtail, hopper, sieve-textured, *etc.*), minerals are chemically zoned and compositional gradients develop in the melt next to the crystal surface (Fig. 5b). Thus the attachment and detachment of atoms at the crystal–melt interface exert a primary control on the diffusion-limited crystal growth which occurs especially if component mobility in the melt is low (*i.e.* low cation diffusivity) owing to high melt viscosity. For the stoichiometric (polymorphic) crystallization of the diopsidic liquid, the effective diffusion mechanism controlling diopside crystal growth is related to the slow diffusivity of Si and O with respect to Ca and Mg ($D_{Ca}, D_{Mg} \gg D_{Si}, D_O$). Silicon and O diffuse at almost the same rate through the melt next to the crystal boundary and their slow mobility is rate-limiting for Ca and Mg (*cf.* Nascimento *et al.*, 2004). Relative to chemical species with weaker cation–oxygen bonds (*i.e.* network-modifier cations), the addition of tetrahedral groups (*i.e.* network-former cations) to the surface of a crystal nucleus is the rate-controlling step of the crystallization reaction. The crystal growth rate is limited by the ability of melt components to diffuse towards or away from the crystallizing front. Chemical elements incompatible in the crystal lattice are rejected by the advancing crystal surface and concentrated in the diffusive boundary layer surrounding the mineral. Unlike long-lived intrusive bodies and metamorphic

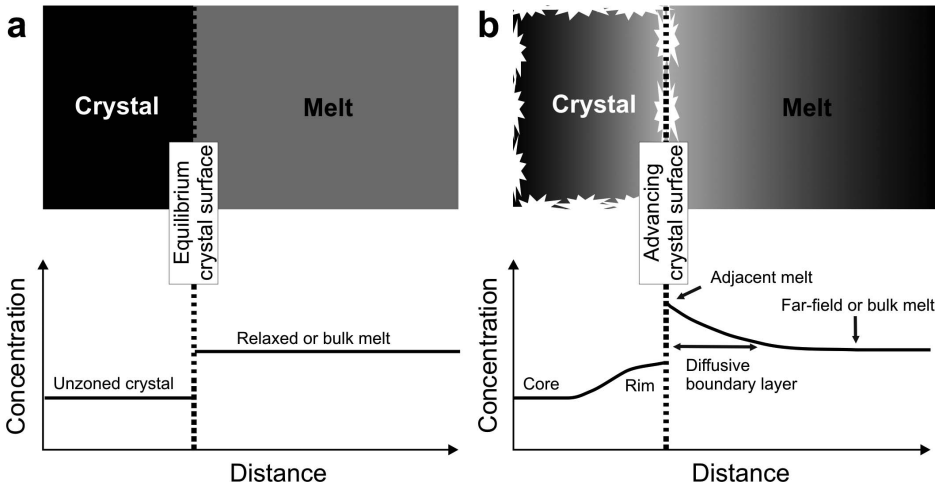


Figure 5. Equilibrium crystallization due to interface-controlled crystal growth (a). The diffusion of chemical elements in the melt prevails over the crystal growth rate. Euhedral and unzoned crystals are surrounded by a compositionally homogeneous melt. Disequilibrium crystallization due to diffusion-controlled crystal growth (b). Rapidly growing crystals are anhedral and chemically zoned, as well as compositional gradients develop in the melt next to the crystal surface.

reactions, fast crystal growth during rapid magma cooling and decompression precludes lattice diffusion as a cause of enrichments of cations in the near-surface or interfacial regions of crystals (e.g. Watson and Liang, 1995).

2.1. Crystal–melt boundary layer vs. olivine chemistry

Several authors investigating basaltic melt compositions (Kushiro, 1974; Kring and McKay, 1984; Kring, 1985; Thornber and Huebner, 1985) observe that diffusion profiles adjacent to rapidly growing olivines are depleted in MgO and FeO, and enriched in CaO, TiO₂, SiO₂ and Al₂O₃ (Fig. 6a). The width of the enrichment and depletion zones decreases in the order MgO > CaO > FeO > TiO₂ > SiO₂ ≈ Al₂O₃, reflecting different cation diffusivities in the melt (e.g. Zhang, 2010). As a first approximation, MgO and FeO in the boundary zone decrease by ~30% and ~10%, respectively, whereas CaO and Al₂O₃ increase by ~10% and ~20%, respectively (Kring, 1985). The diffusive boundary layer is prevalently depleted in MgO rather than FeO, suggesting that the melt more easily supplies fresh Fe cations to the advancing crystal surface (i.e. $D_{\text{Fe}} > D_{\text{Mg}}$). Similarly, the smaller increase of CaO relative to Al₂O₃ and SiO₂ at the crystal–melt interface indicates that the mobility of Ca in the melt is faster than that of network-former cations (i.e. $D_{\text{Ca}} > D_{\text{Al}}$). This diffusion-controlled process is corroborated by dynamic experiments conducted on a trachybasalt cooled from the liquidus down to 1150, 1125 and 1000°C at 1 and 900°C/h (Conte *et al.*, 2006). As the quench temperature decreases, the concentration of MgO in olivine decreases, counterbalanced by increasing FeO and CaO contents (Fig. 6b). In contrast, the

2.2. Crystal–melt boundary layer vs. clinopyroxene chemistry

In the late 1970s and early 1980s, many laboratory studies were conducted to better understand the influence of undercooling on clinopyroxene textural and compositional variations (Lofgren *et al.*, 1974; Walker *et al.*, 1976; Grove and Bence, 1977; Grove and Raudsepp, 1978; Gamble and Taylor, 1980; Shimizu, 1981; Kouchi *et al.*, 1983; Baker and Grove, 1985; Tsuchiyama, 1985). The overall finding was that departure from equilibrium arises mainly because of a difference in the rate of crystal–melt interface advance and the rate of chemical diffusion in the melt. In cases where clinopyroxene was surrounded by homogeneous melt, suggesting interface-control over crystal growth, the sluggishness of short-range diffusion of Al was nevertheless capable of causing disequilibrium in the solid (Grove and Raudsepp, 1978; Gamble and Taylor, 1980; Mollo *et al.*, 2010, 2012b). This result is explained by the presence of a thin diffusive boundary layer enriched in chemical species less compatible in clinopyroxene (*i.e.* Al_2O_3 , TiO_2 and Na_2O), and relatively depleted in highly compatible chemical elements (*i.e.* FeO , CaO and MgO) (Fig. 7a). Concentration-dependent partitioning produces clinopyroxene growth layers that respond to the chemical gradients in the melt, producing compositions that are progressively enriched in $^{\text{IV}}\text{Al}$, Ti and Na and depleted in Fe^{2+} , Ca and Mg with increasing cooling rate (Fig. 7b). Therefore, under dynamic crystallization conditions, diopside (Di: $\text{MgCaSi}_2\text{O}_6$) and hedenbergite (Hd: $\text{FeCaSi}_2\text{O}_6$) components both decrease, whereas the opposite occurs for ferrosilite (Fs: FeSiO_3), enstatite (En: MgSiO_3), jadeite (Jd: $\text{NaAlSi}_2\text{O}_6$), and calcium-, ferri- and titanium-Tschermak components (Ts: $\text{CaAl}_2\text{SiO}_6$, $\text{CaFe}_2\text{SiO}_6$ and $\text{CaTiAl}_2\text{O}_6$, respectively), summarized in the scheme:

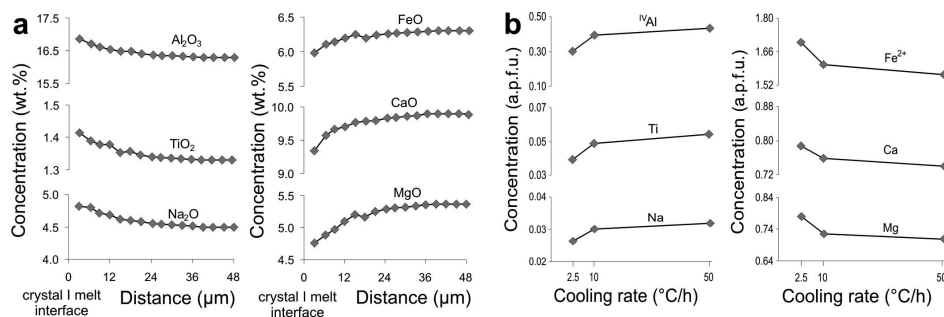
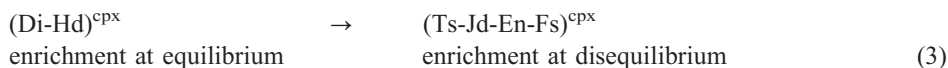


Figure 7. During rapid growth of clinopyroxene, the diffusive boundary layer in the melt is enriched in chemical species incompatible with the crystal lattice (*i.e.* Al_2O_3 , TiO_2 and Na_2O), whereas the concentrations of compatible chemical elements decrease (*i.e.* FeO , CaO and MgO) (a). Disequilibrium clinopyroxene crystals are progressively enriched in $^{\text{IV}}\text{Al}$, Ti and Na counterbalanced by depletions in Fe^{2+} , Ca and Mg with increasing cooling rate (b). After Mollo *et al.* (2013c) in which a trachybasalt was cooled at atmospheric pressure using cooling rates of 2.5, 10 and $50^{\circ}\text{C}/\text{h}$ from 1250°C down to 1100°C . A superliquidus temperature (1250°C) was reached starting from room temperature (with a heating ramp of $100^{\circ}\text{C}/\text{min}$), and it was maintained for 30 min before the start of cooling. If not observable, error bars are within symbols.



According to equation 3, clinopyroxene chemistry is controlled by the substitution of $M^2(\text{Mg}, \text{Fe}^{2+})$ with $M^1(\text{Al}, \text{Fe}^{3+})$ coupled with the substitution of Si with Al in the tetrahedral site to form the Tschermak components. Highly charged cations, such as titanium and trivalent iron, are accommodated in the $M1$ site of clinopyroxene to balance the charge deficiency caused by the increasing concentration of aluminium (Mollo *et al.*, 2013a). In naturally cooled clinopyroxenes, remarkable TiO_2 and Al_2O_3 enrichments have been recognized as a response to rapid crystal growth caused by heat dissipation at the chilled margins of dykes (Ujike, 1982; Mollo *et al.*, 2011b; Scarlato *et al.*, 2014) and the outermost parts of lava flows (Mével and Velde, 1975; Coish and Taylor, 1979; Mollo *et al.*, 2015), as well as during fast cooling of extraterrestrial materials like lunar basalts (Schnare *et al.*, 2008) and basaltic meteorites (Mikouchi *et al.*, 1999).

2.3. Crystal–melt boundary layer vs. plagioclase chemistry

More than perhaps any other magmatic mineral, plagioclase is characterized by marked sensitivity to pressure, temperature and changes in the concentration of H_2O dissolved in the melt. The kinetics of CaAl–NaSi intracrystalline diffusion is extremely slow (Tsuchiyama, 1985) and, consequently, diffusive chemical equilibration for plagioclase crystals 1 to 100 mm in size may require durations longer than the typical lifetimes of magma chambers. Since whole-crystal equilibration by subsolidus diffusion is virtually impossible for plagioclase, the ubiquitous core-to-rim compositional variations observed in natural crystals record the physicochemical perturbations of the magmatic systems. For this reason, numerous cooling and decompression studies explore the effect of undercooling and magma mixing on the crystallization kinetics of plagioclase (Kirkpatrick *et al.*, 1976; Corrigan, 1982; Smith and Lofgren, 1983; Muncill and Lasaga, 1987, 1988; Sato, 1995; Hammer and Rutherford, 2002; Couch, 2003; Pupier *et al.*, 2008; Iezzi *et al.*, 2008, 2011, 2014; Brugger and Hammer, 2010a, 2015; Mollo *et al.*, 2011a,b). If crystal growth-rate is large compared with the rate of component diffusion in the melt, a diffusive boundary layer depleted in compatible elements (Ca and Na), and enriched in relatively incompatible elements (Mg and Fe) results (Fig. 8a). Additionally, the strength of the Si–O bonds in the melt (443 kJ/mol) is greater than that of Al–O bonds (330–422 kJ/mol) due to the influence of charge-balancing metal cations (*e.g.* Ca, Na, *etc.*) on the bonding forces of aluminium in tetrahedral coordination and the lower charge of Al^{3+} compared to Si^{4+} (Kirkpatrick, 1983). This difference in bonding energy means that the transfer rates of Al cations from the melt to the surface of rapidly growing crystals is facilitated more than that of Si cations (Iezzi *et al.*, 2011, 2014). Under diffusion-controlled crystal-growth conditions, Si-rich plagioclases are therefore delayed with respect to Si-poor ones, favouring systematic Al enrichments in the crystal lattice (Iezzi *et al.*, 2014). Although the melt supplies Na cations to the advancing plagioclase surface at rates faster than Ca ($D_{\text{Na}} > D_{\text{Ca}}$), the transport of Al across the crystal–melt interface is rate-limiting for the growth of plagioclase. In order

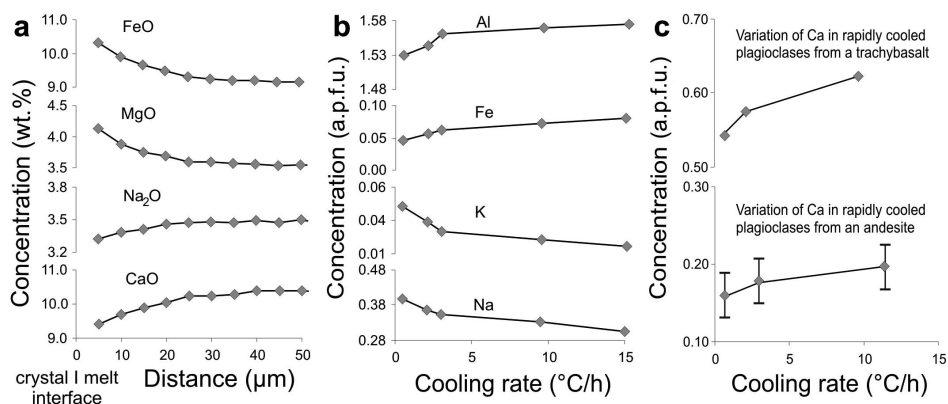


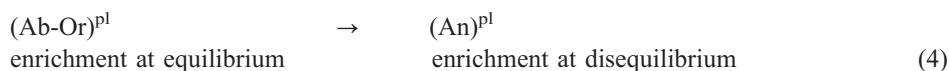
Figure 8. The disequilibrium growth of plagioclase is associated with the development of a diffusive boundary layer in the melt depleted in Ca and Na, and enriched in Mg and Fe (a). The plagioclase crystal lattice is progressively depleted in Si, Na and K, and enriched in Al, Ca, Fe and Mg (b). After Mollo *et al.* (2011a) in which a trachybasalt was held at 500 MPa and a superliquidus temperature of 1250°C for 30 min, and then cooled using cooling rates of 15, 9.4, 3, 2.1 and 0.5°C/min from 1250°C down to 1000°C. Variation of Ca in rapidly cooled plagioclases from trachybasalt and andesitic melts (c). If trachybasaltic and andesitic melts are cooled at comparable rates, plagioclases from the more viscous andesitic liquid become mantled by thick diffusive boundary layers that impinge upon one another as crystallization proceeds. As a consequence, each single crystal competes with its near neighbours for chemical nutrients. For a single cooling rate, calcium in andesitic plagioclases shows variations much greater than those observed for trachybasaltic crystals. Data from Mollo *et al.* (2011a) and Iezzi *et al.* (2014) in which an andesite was held at atmospheric pressure and 1300°C, and then cooled at 12.5, 3 and 0.5°C/min to the final quenching temperature of 800°C. If not observable, error bars are within symbols.

to compensate for the cation-charge imbalance due to Al-Si substitution, plagioclase becomes preferentially enriched in Ca rather than Na, also incorporating Fe and Mg at non-stoichiometric proportions (Mollo *et al.*, 2011a).

Undercooling exerts a powerful control on the composition of plagioclase crystals. Consequently, the ions available for uptake by growing plagioclase causes Si, Na and K to decrease progressively in plagioclase, whereas Al, Ca, Fe and Mg increase (Fig. 8b). However, with respect to primitive magmas, cooling and decompression experiments conducted on more evolved andesitic and rhyodacitic melts (quenched at relatively low temperatures) have indicated strong calcium variations in plagioclases formed from the same charge (Brugger and Hammer, 2010a; Iezzi *et al.*, 2014). It is apparent that the compositional variability of plagioclase depends on the magnitude of concentration gradients in the melt, which in turn scale with undercooling. On the other hand, the diffusivity of chemical elements scales with the melt viscosity that, in turn, changes as a function of melt differentiation and temperature. A thick diffusive boundary layer develops more favourably around crystals growing from high-viscosity (and/or low-temperature) melts and this thickness gradually increases as long as crystallization continues (Watson and Müller, 2009). The combination of an enlarged boundary layer and a fast growth rate may overwhelm the control of linear cooling rate on mineral

chemistry leading to the formation of highly heterogeneous crystals. If trachybasaltic and andesitic melts are cooled at comparable rates, plagioclases from the more viscous andesitic liquid become mantled by thick diffusive boundary layers that impinge upon one another as crystallization proceeds. Diffusion effects extend completely across the melt regions among growing plagioclases so that each single crystal competes with its near neighbours for chemical nutrients. This competitive-diffusion mechanism is more intense where plagioclases cluster in close proximity to one another, but is less intense where crystals are relatively widely and evenly spaced. As a consequence, for a single cooling rate, calcium in andesitic plagioclases shows variations much greater than those observed for trachybasaltic crystals (Fig. 8c).

Experimentally derived plagioclase compositions also indicate that the rearrangement of the Al-Si tetrahedral framework and the occurrence of more calcic crystals both imply that the amount of anorthite component (An: $\text{CaAl}_2\text{Si}_2\text{O}_8$) increases at the expense of albite (Ab: $\text{NaAlSi}_3\text{O}_8$) and orthoclase (Or: KAlSi_3O_8) through the scheme (Mollo *et al.*, 2011b):

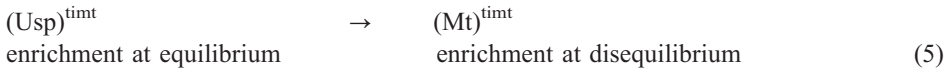


It is interesting to note that the direction of equation 4 is the same, regardless of whether cation redistributions are driven by equilibrium or disequilibrium crystallization conditions. Indeed, increasing temperature and/or melt-water concentration reduce the activity of both Ab and Or relative to An in plagioclase. Therefore, in naturally cooled magmas, it may be difficult to distinguish effects of disequilibrium that are induced by rapid growth rate from effects of closed-system crystallization, which have an identical influence on plagioclase components (Singer *et al.*, 1995; Kent *et al.*, 2010). The difficulty of assessing and quantifying disequilibrium growth of plagioclase can be mitigated by considering the non-stoichiometric uptake of incompatible elements (*e.g.* Mg and Fe) and/or detailed crystal textural analyses. For example, core-to-rim compositional profiles in plagioclase phenocrysts are important for distinguishing thermally and chemically closed magmatic systems from open systems, constraining patterns of magmatic heat loss and convection, and quantifying the rates at which magma ascent occurs. In this framework, abrupt increases in Mg and Fe measured in plagioclase phenocrysts may reveal episodes of rapid disequilibrium due to undercooling at pre-eruptive magma chamber conditions and/or during magma ascent to the surface (Singer *et al.*, 1995).

2.4. Crystal–melt boundary layer vs. titanomagnetite chemistry

Only a few laboratory studies have investigated the effect of undercooling on the crystallization of accessory minerals typical of igneous rocks, such as titanomagnetite (Mollo *et al.*, 2012a,b). The rapid growth of titanomagnetite is closely related to the development of a diffusive boundary layer enriched in Al_2O_3 and MgO, and depleted in

TiO₂ and FeO (Fig. 9a). These latter components are both compatible in titanomagnetite, but chemical diffusion does not supply Ti and Fe to the advancing crystal surface at the same rate (*i.e.* $D_{\text{Fe}} > D_{\text{Ti}}$). Consequently, TiO₂ is observed to decrease drastically by ~50% in the diffusive boundary layer, whereas FeO increases by only ~10%. This disequilibrium fractionation between Ti and Fe leads to the growth of TiO₂-poor titanomagnetite crystals (Fig. 9b), showing Ti/Fe_{tot}²⁺ ratios that gradually decrease as a function of undercooling (*e.g.* Zhou *et al.*, 2000). Since magmatic titanomagnetites exhibit a complete solid solution between magnetite (Mt: Fe₃O₄) and ulvöspinel (Usp: Fe₂TiO₄) end-members, this kinetically controlled cation redistribution can be expressed as:



It is worth stressing that the Usp-Mt replacement described by equation 5 parallels the preferential stability of Mt during equilibrium crystallization of titanomagnetite at higher temperature, except that it is more exaggerated (Mollo *et al.*, 2013b). By analogy with the disequilibrium growth of plagioclase discussed above, the incorporation of Al and Mg cations into the titanomagnetite crystal lattice is the best evidence of departure

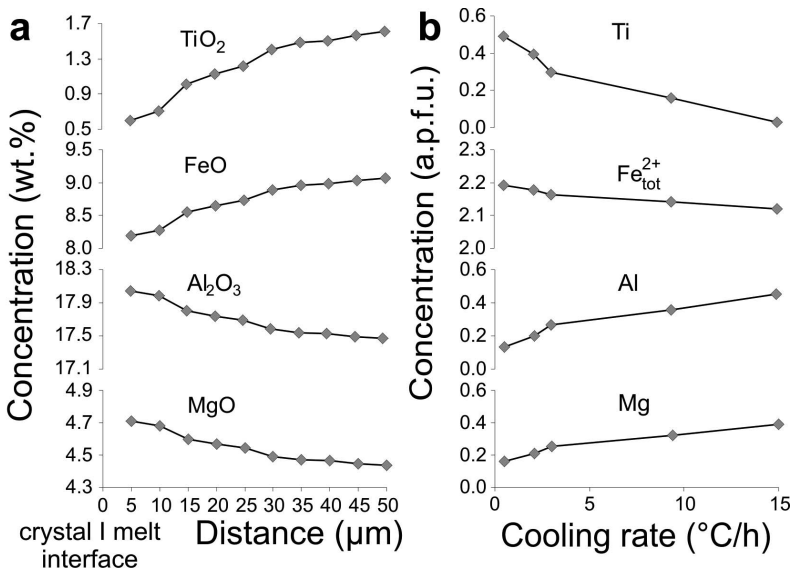


Figure 9. The rapid growth of titanomagnetite leads to the development of a diffusive boundary layer enriched in Al₂O₃ and MgO, and depleted in TiO₂ and FeO (a). After Mollo *et al.* (2013b) in which a trachybasalt was held at 500 MPa and a superliquidus temperature of 1250°C for 30 min, and then cooled using cooling rates of 15, 9.4, 3, 2.1 and 0.5°C/min from 1250°C down to 1000°C. With increasing cooling rate, Ti and Fe decrease in the titanomagnetite crystal lattice, whereas Al and Mg increase (b). Data from Mollo *et al.* (2013b). If not observable, error bars are within symbols.

from equilibrium under diffusion-controlled crystal growth conditions (Fig. 9b). It is not a coincidence that euhedral Ti-rich, Al-Mg-poor titanomagnetites are found generally in the innermost and less efficiently cooled parts of dykes and lavas, whereas anhedral Ti-poor, Al-Mg-rich crystals characterize the outermost and rapidly cooled portions (Zhou *et al.*, 2000; Mollo *et al.*, 2011b).

3. Effect of crystal growth rate on element partitioning

When crystal growth shifts from interface-controlled to diffusion-controlled the transport of chemical elements in the melt is not sufficiently rapid to supply nutrients in the same proportion as exists in the far-field melt. A diffusive boundary layer develops in the melt adjacent to the crystal surface showing composition different from that of the bulk melt far from the crystal surface where chemical gradients cease and the system returns to homogeneous concentrations. An important consequence of this process is that the partition coefficient measured between the advancing crystal surface and the diffusive boundary layer interface changes substantially with the effect of chemical gradients in the melt. The partition coefficient is expressed as:

$$K_i = C_i^{\text{xls}}/C_i^{\text{melt}} \quad (6)$$

where C_i^{xls} is the concentration of a chemical element i in the crystal and C_i^{melt} is the concentration of the same element in the melt (both crystal and melt concentrations expressed as wt.%). In order to understand better some magmatic reactions, it is also convenient to use the exchange partition coefficient that represents the partitioning of two elements, i and j , between crystal and melt:

$$K_d(i-j)^{\text{xls-melt}} = K_i/K_j = (C_i^{\text{xls}}/C_i^{\text{melt}})/(C_j^{\text{xls}}/C_j^{\text{melt}}) = (C_i/C_j)^{\text{xls}}/(C_i/C_j)^{\text{melt}} \quad (7)$$

When the compositions of both crystal and melt result from interface-controlled growth and are supposed to be in equilibrium with respect to element exchange at the crystal–melt interface, equations 6 and 7 provide the ‘true’ (or ‘actual’ or ‘real’) partition coefficient K_i^{true} . In contrast, the effect of diffusion-controlled growth is to change K_i^{true} in an ‘apparent’ (or ‘effective’) partition coefficient K_i^{app} when the chemistry of the advancing crystal surface reflects the chemical concentrations in the diffusive boundary layer rather than the composition of the original bulk melt. It is surprising to find that, in studies dealing with magmatic processes, K_i^{app} is calculated as the ratio between: (1) the concentrations of an element at a given analytical spot on the crystal and matrix glass; (2) the compositions of a crystal rim and residual glass unaffected by chemical gradients; and (3) the averaged chemistry of a zoned crystal and the composition of the host melt represented by the bulk-rock analysis. Apart from this variety of calculation methods, Albarede and Bottinga (1972) provided the most complete definition for K_i^{app} , as each possible partition coefficient that differs from the value measured “between a freshly deposited crystalline layer and the portion of the melt right adjacent to this layer”. Thus, during development of diffusion-controlled

reactions, the simple partition coefficient K_i calculated exactly at the crystal–melt interface will represent the condition in which the advancing crystal surface is in near local equilibrium with the adjacent melt. When a steady state condition is achieved at the crystal–melt interface, both breakage and formation of chemical bonds proceed at the same rate, irrespective of the ever-changing compositions of the zoned crystal and diffusive melt layer. Any other situation will invariably lead to the attainment of an infinite number of K_i^{app} that more or less approximate to K_i^{true} , depending on the relative magnitudes of the crystal growth rate and chemical diffusivity in the melt. It is also expected that fast-diffusing species will show the least difference between K_i^{app} and K_i^{true} , whilst slow-diffusing species will show the greatest difference. Taking all of the above into account, in the present usage the term K_i refers to the measurement of element partitioning between crystal rim and coexisting melt (*i.e.* element partitioning at the crystal–melt interface), besides the fact that a certain uncertainty may be introduced by the spatial resolution of the analytical spot size.

3.1. Olivine–melt partitioning

Using experimental data from Conte *et al.* (2006), the partitioning of Mg, Fe and Ca between rapidly growing olivine crystals and a trachybasaltic melt have been calculated. Figure 10a shows that K_{Mg} , K_{Fe} and K_{Ca} increase by ~3%, ~10% and ~30%, respectively, with increasing cooling rate. Calcium is highly incompatible with olivine and its concentration rises in the contacting melt. The composition of the advancing crystal surface parallels the gradual Ca enrichment of the melt leading to a substantial increase in K_{Ca} as a function of cooling rate. Although both Mg and Fe are compatible in olivine, the increase observed for K_{Fe} is greater than that measured for K_{Mg} due to the preferential supply of fresh Fe cations from the melt to the advancing crystal surface. It is interesting to observe that the value of $K_d(\text{Fe–Mg})^{\text{ol–melt}}$ does not change substantially at fast cooling rates (Fig. 10a), remaining close to the equilibrium range of 0.30 ± 0.03 estimated for equilibrium crystallization conditions (Roeder and Emslie, 1970; Falloon *et al.*, 2007). Comparable equilibrium values ranging from 0.27 to 0.33 were also found unexpectedly in cooling-rate studies conducted on lunar basalts (Walker *et al.*, 1976; Powell *et al.*, 1980; Kring and McKay, 1984), and terrestrial trachybasalts and basaltic andesites (Baker and Grove, 1985; Conte *et al.*, 2006).

Petrologists and volcanologists often use the Fe–Mg exchange to ascertain whether the olivine–melt pairs chosen for modelling of magmatic processes were in equilibrium at the time of crystallization. However, the fact that the value of $K_d(\text{Fe–Mg})^{\text{ol–melt}}$ remains almost constant upon kinetic effects raises many questions about the fidelity of Fe–Mg exchange as a test for true multicomponent equilibrium crystallization and interface-controlled growth. Several motivations have been proposed to explain the tendency of olivine to maintain Fe–Mg equilibrium with the surrounding melt. In natural magmas, olivine is generally the liquidus phase and saturates the melt at a relatively high temperature and low degree of crystallization. The melt viscosity is low and chemical species diffuse quickly. The kinetic growth of olivine occurs in a restricted thermal path that is fairly close to the near-liquidus region of the melt

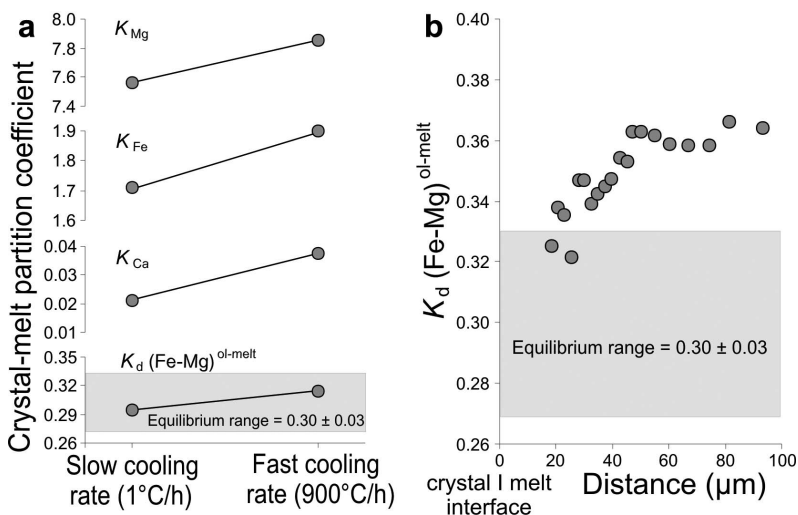


Figure 10. K_{Mg} , K_{Fe} , K_{Ca} and $K_d(Fe-Mg)^{ol-melt}$ measured at the interface between olivine crystals and a trachybasaltic melt are found to increase with increasing cooling rate (a). Notably, the value of $K_d(Fe-Mg)^{ol-melt}$ does not change substantially at fast cooling rates, falling into the equilibrium range of 0.30 ± 0.03 . Data from Conte *et al.* (2006) in which a trachybasalt was melted for 3 h above the liquidus temperature, then cooled to 1150, 1125 and 1100°C at linear cooling rates of 900°C/h (fast cooling rate) or 1°C/h (slow cooling rate), then held at these temperatures for 12 h, and finally quenched at atmospheric pressure. $K_d(Fe-Mg)^{ol-melt}$ measured at the crystal–melt interface most closely approaches the equilibrium range but its value increases progressively towards disequilibrium levels as the glass farther and farther from the interface is used for the calculation (b). Data from Powell *et al.* (1980) in which a basalt was cooled from 1198 to 1050°C with a cooling rate of 64°C/h, and then quenched at atmospheric pressure. If not observable, error bars are within symbols.

corresponding to a few degrees of crystallization. These factors suggest that, at the early stage of olivine crystallization, the fresh molecular layer deposited on the surface of a growing crystal maintains Fe-Mg partitioning equilibrium with the contacting melt. Apparently, the development of a boundary layer favours local interface equilibrium (*i.e.* equilibrium of a reaction in a small volume) rather than kinetic effects due to diffusion-limited reactions. The crystal surface remains in equilibrium with the host melt through steady-state chemical gradients established at the onset of olivine nucleation, so that local equilibrium is maintained persistently in terms of Fe-Mg exchange between the advancing crystal surface and the diffusive boundary layer (Kring and McKay, 1984). This is confirmed by microprobe analytical traverses across a basaltic glass surrounding olivine crystals cooled rapidly at 64°C/h from 1198°C to 1050°C (Powell *et al.*, 1980). While the value of $K_d(Fe-Mg)^{ol-melt}$ measured at the crystal–melt interface approaches most closely the equilibrium range, the exchange partition coefficient is found to increase progressively towards disequilibrium levels as the glass further and further from the interface is used for the calculation (Fig. 10b). Interestingly, the skeletal and dendritic morphologies of rapidly growing olivine

crystals (Faure *et al.*, 2003, 2007), and strong evidence for early dendritic morphology from phosphorus enrichments (Milman-Barris *et al.*, 2008; Welsch *et al.*, 2014) indicate that the advance of the solid–liquid interface is not within the interface-controlled regime, as explained by stability theory (Mullins and Sekerka, 1963). Small perturbations at the interface generate protrusions from the crystal that are exposed to slightly higher nutrient concentration, promoting their accelerated growth in a positive feedback. Further penetration of the boundary layer by the protrusion supplies fresh chemical components without the need for long-range chemical diffusion (Walker *et al.*, 1976). Evidently, morphologic manifestation of diffusion control is decoupled from Fe–Mg exchange equilibrium, perhaps because these elements are less unlikely to be fractionated by differences in melt diffusivity within the boundary layer.

3.2. Clinopyroxene–melt partitioning

The Fe–Mg exchange is also used as a test for equilibrium for the crystallization of clinopyroxene from magma. The equilibrium value of $K_d(\text{Fe–Mg})^{\text{cpx–melt}}$ is assumed to be in the range of 0.27 ± 0.03 , but is not perfectly invariant due to a slight temperature dependency (*cf.* Putirka, 2008). As for the case of olivine, the Fe–Mg exchange cannot be assumed to be a reliable indicator of clinopyroxene–melt equilibrium due to the fact that diffusion-controlled compositions yield a fairly close correspondence of $K_d(\text{Fe–Mg})^{\text{cpx–melt}}$ to the equilibrium range (Baker and Grove, 1985; Conte *et al.*, 2006; Mollo *et al.*, 2010, 2012b). With increasing cooling rate, Mollo *et al.* (2013a) found that the Fe–Mg exchange coefficient measured at the crystal–melt interface depicts an asymptotic trend fitted by an exponential rise to a maximum model (Fig. 11a). This suggests that the increasing K_{Fe} and K_{Mg} values inevitably tend towards an almost constant $K_{\text{Fe}}/K_{\text{Mg}}$ ratio when the crystal growth rate is much greater than the mobility of both Fe and Mg in the melt. The constancy of $K_d(\text{Fe–Mg})^{\text{cpx–melt}}$ reflects the achievement of local interface equilibrium, especially at high temperature where clinopyroxene nucleation and growth occurs close to the near-liquidus region of magma.

The development of local equilibrium interface reactions also supports the hypothesis that incorporation of rare earth elements (*REE*) into rapidly growing clinopyroxene is controlled by the local charge-balanced configurations, bearing in mind the extent of disorder across the *M1*, *M2* and *T* sites (Mollo *et al.*, 2013c). As clinopyroxene crystals grow more rapidly in response to increasing cooling rate, values of K_{REE} increase systematically (Fig. 11b) together with K_{Al} and K_{Na} , whereas K_{Si} and K_{Ca} decrease (Fig. 11c). The entry of *REE* into the *M2* site is facilitated by a coupled substitution where either Na substitutes for Ca on the *M2* site or $^{\text{IV}}\text{Al}$ substitutes for Si in the tetrahedral site (Blundy *et al.*, 1998; Wood and Blundy, 2001). This latter substitution reflects an increased ease of locally balancing the excess charge at *M2* as the number of surrounding $^{\text{IV}}\text{Al}$ atoms increases (Hill *et al.*, 2000). Due to the lower concentration of Ca in rapidly cooled clinopyroxenes, divalent large ion lithophile elements (LILE) on *M2* decrease (*i.e.* Ca, Sr and Ba) in concert with a concomitant increase of monovalent cations (*i.e.* Li, Na, Rb). This causes a decoupling effect

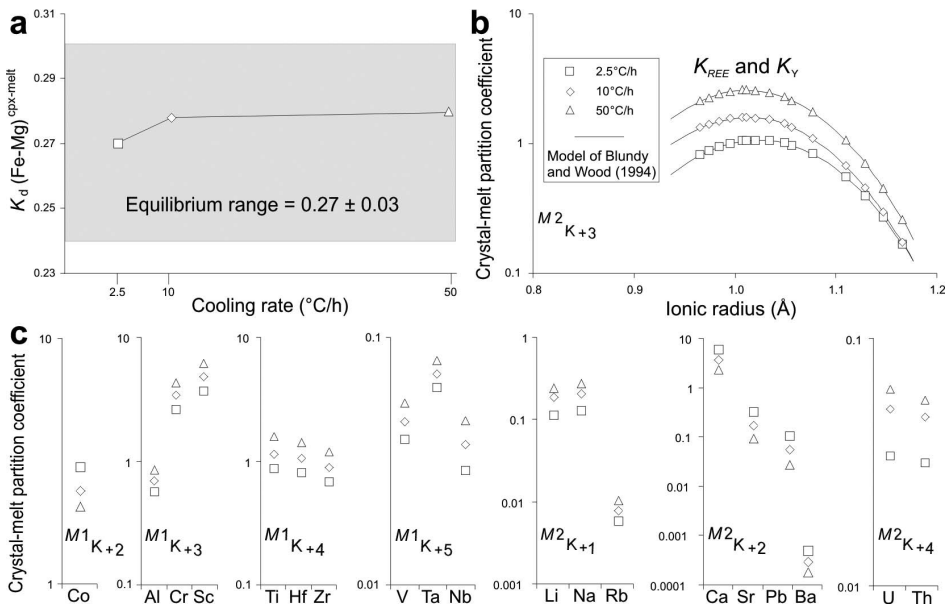


Figure 11. As the cooling rate is increased, the Fe–Mg exchange coefficient, *i.e.* $K_d(\text{Fe–Mg})^{\text{cpx–melt}}$, tends to increase to a maximum value that closely agrees with the equilibrium range of 0.27 ± 0.03 (a). After Mollo *et al.* (2013a) in which a trachybasalt was cooled at atmospheric pressure using cooling rates of 2.5, 10 and 50 $^{\circ}\text{C/h}$ from 1250 $^{\circ}\text{C}$ down to 1100 $^{\circ}\text{C}$. Plots of partition coefficients for REE and Y vs. ionic radii as a function of cooling rate (b). The lines show fits to the lattice strain model of Blundy and Wood (1994). After Mollo *et al.* (2013c) in which the starting composition and experimental conditions are the same as reported above. Partition coefficients for trace elements in the $M1$ and $M2$ sites of clinopyroxene as a function of cooling rate (c). Elements are grouped by ionic charge and arranged from smallest to largest ionic radius within each group. After Mollo *et al.* (2013c). If not observable, error bars are within symbols.

between partition coefficients for monovalent and divalent cations where K_{LILE} decrease and increase simultaneously with increasing cooling rate as a function of the cation charge (Fig. 11c). Conversely, high-field-strength elements enter the $M1$ (HFSE; *i.e.* Ti, Zr, Nb and Ta) and K_{HFSE} show a net increase as average charge on this site increases. Charge imbalances are caused by increasing Ca–Al–Tschermak ($\text{CaAl}_2\text{SiO}_6$) and Ca–ferri–Tschermak ($\text{CaFe}_2\text{SiO}_6$) substitutions driven by replacement of Mg^{2+} by Fe^{3+} and Al^{3+} into the octahedral site (Wood and Trigila, 2001). Therefore, to maintain charge balance, K_{HFSE} tends always to increase in rapidly cooled clinopyroxenes (Fig. 11c). Upon kinetic effects, the concentration of trivalent transition elements (TE) into the $M1$ site also increases (*i.e.* Cr and Sc), accompanied by greater $^{\text{VI}}\text{Al}$ content in the same structural site and the substitution of $^{\text{M2}}\text{Fe}^{2+}$ for $^{\text{M1}}\text{Fe}^{3+}$ (Mollo *et al.*, 2013c). Although both K_{Cr} and K_{Sc} increase with increasing cooling rate, K_{Co} shows the opposite behaviour. However, the $M1$ site requires an increased net charge (from 2+ to 3+) to balance the overall increase in aluminium (Hill

et al., 2000) and, consequently, trivalent-charged TE cations are incorporated preferentially over divalent ones. It is worth noting that, using the Onuma diagram (Onuma *et al.*, 1968) for REE and Y, partition coefficients of isovalent cations vs. ionic radius lie on parabola-like curves irrespective of equilibrium or dynamic crystallization conditions (Fig. 11b). In the Onuma diagram, the peak position of the parabola is due to the control of crystal structure on trace-element partitioning where the crystal structure (*i.e.* the size of the site occupied by the cation) is correlated with the crystal composition. As the cooling rate increases, ^{IV}Al in clinopyroxene increases and the parabola shifts upward, opens up more and becomes wider. The lattice strain in the crystal has been identified as the cause of this parabolic trend and Blundy and Wood (1994) provided a quantitative expression relating the variation in K_i with ionic radius to the physical properties of the host crystal. In the lattice strain model, the partitioning of a substituent cation (radius r_i in metres) onto a structural site is related to the site radius (r_0), its apparent Young modulus (E in GPa), and the strain-free partition coefficient K_0 for a fictive cation with radius r_0 :

$$K_i = K_0 \exp\{-4\pi N_A [r_0/2(r_i - r_0)^2 + 1/3(r_i - r_0)^3]/(RT)\} \quad (8)$$

where N_A is Avogadro's number ($6.022 \times 10^{23} \text{ mol}^{-1}$), R is the universal gas constant ($8.3145 \times 10^3 \text{ kJ mol}^{-1}$), and T is the temperature (in Kelvin). There is good agreement between the partition coefficients predicted by equation 7 and those measured at both equilibrium and cooling-rate conditions (Fig. 11b). It is also found that the calculated value of r_0 exhibits a weak negative correlation with ^{IV}Al content, whereas K_0 and E increase significantly determining, respectively, the increasing height and curvature of the partitioning parabola (Mollo *et al.*, 2013c). It is important to note that Wood and Blundy (1997) developed also a method of predicting variations in partition coefficients using thermodynamic principles in combination with the lattice strain model. In practice, all REE and Y trends depicted in Fig. 11b can be described rigorously thermodynamically and are hence equally valid whether or not the growth of clinopyroxene is driven by equilibrium or disequilibrium exchanges. In light of the lattice strain model, kinetically controlled major cation substitution reactions affect K_i through charge-balance mechanisms comparable to those observed during equilibrium partitioning. Therefore, deviations from equilibrium partitioning are insufficient to change the ability of a trace element to be compatible (or incompatible) within the clinopyroxene crystal lattice and the measured partition coefficient is of the same order of magnitude as the equilibrium value (Fig. 11b). In other words, upon the effect of rapid crystal-growth conditions, local chemical equilibrium at the crystal–melt interface responds to the increasing probability of trace cations entering a locally charge-balanced site when the major cation concentrations change (Mollo *et al.*, 2013c). Rationally, as local equilibrium is achieved between rapidly growing clinopyroxene crystals and coexisting melts, cation substitution reactions can be treated in terms of the energetics of the various charge-imbalanced configurations (*cf.* Wood and Blundy, 2001). For the sake of completeness, it is worth stressing that trace-element partition coefficients many

orders of magnitude greater than the equilibrium values have been measured during rapid growth of olivine and clinopyroxene. Pinilla *et al.* (2012) noted that lattice discontinuities or defects of all types (*e.g.* voids and channels) at crystal grain boundaries may serve as important storage sites for trace elements, although most trace elements remain incompatible in the bulk crystal lattice because of unfavourable incorporation energies. Additionally, Kennedy *et al.* (1993) documented that rapidly growing crystals may entrap small portions of the diffusive boundary layer that are found as minute melt inclusions randomly distributed in the mineral phase. However, under such circumstances, any form of trace-element uptake cannot be ascribed to the achievement of local chemical equilibrium. Charge-balanced configurations and the lattice-strain model are substantially inapplicable, and regular relationships between the ionic radius, the valence of the trace element, and the partition coefficient are never found.

3.3. Plagioclase–melt partitioning

In the case of plagioclase, dynamic crystallization experiments reproducing magma cooling and decompression have shown that the partition coefficients of compatible and incompatible elements may deviate from the equilibrium values in proportion to the rates of environmental change (Brugger and Hammer, 2010a; Mollo *et al.*, 2011a). For example, during crystallization of a trachybasaltic melt, K_{Ca} , K_{Na} and K_K are observed to decrease with increasing cooling rate, whereas K_{Fe} , K_{Mg} and K_{Al} increase significantly (Mollo *et al.*, 2011a). This is interpreted to be a consequence of the incompatible character of Fe and Mg in plagioclase causing build-up in a boundary layer and the slow progress of Al across the crystal–melt interface that is rate-limiting for the crystal growth (Fig. 12a). Using the lattice-strain model and thermodynamic principles, Dohmen and Blundy (2014) demonstrate that K_{Ca} and K_{Na} have a strong control on the partitioning behaviour of trace elements between plagioclase and melt. For a wide range of plagioclase and melt compositions, K_{Sr} increases with decreasing K_{Ca} , although Sr substitutes for Ca in plagioclase during magmatic processes. This apparent anomaly is explained in part by the greater elasticity of the albite lattice in which larger Sr cations are more easily accommodated with respect to anorthite-rich plagioclases (Blundy and Wood, 1991). It is important to note that Singer *et al.* (1995) observed that the inverse relationship between K_{Sr} and K_{Ca} is still valid for disequilibrium plagioclase phenocrysts formed from naturally cooled dacitic magmas. The authors modelled the progressive change of K_{Sr}^{app} due to the development of a hypothetical diffusive boundary layer in the melt adjacent to the rapidly growing crystal. K_{Sr}^{app} is expressed as the ratio of the concentration of Sr at a given analytical spot on the crystal to the concentration of Sr in the bulk melt (*i.e.* the bulk-rock analysis). Furthermore, the authors model the variation of K_{Sr}^{app} assuming that the advance of the crystal–melt interface into the crystal-poor dacitic melt does not violate the condition of crystal growth into a non-convecting infinite melt reservoir (Smith *et al.*, 1955):

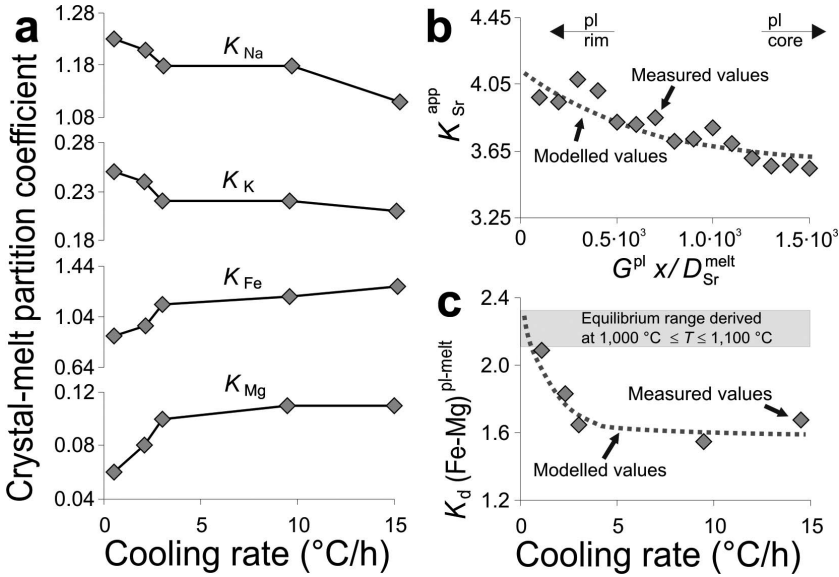


Figure 12. Element partitioning between plagioclase and melt showing that K_{Ca} , K_{Na} and K_K decrease with increasing cooling rate, whereas K_{Fe} , K_{Mg} , and K_{Al} increase (a). After Mollo *et al.* (2011a) in which a trachybasalt was held at 500 MPa and a superliquidus temperature of $1250^\circ C$ for 30 min, and then cooled using cooling rates of 15, 9.4, 3, 2.1 and $0.5^\circ C/min$ from $1250^\circ C$ down to $1000^\circ C$. Progressive change of K_{Sr}^{app} due to the development of a hypothetical diffusive boundary layer in the melt adjacent to the rapidly growing plagioclase rim (b). Values ‘modelled’ using equation 9 and ‘measured’ for K_{Sr}^{app} are aligned along two almost identical trends, confirming the disequilibrium growth of plagioclase due to magma undercooling. Data from Singer *et al.* (1995). The value of $K_d(Fe-Mg)^{pl-melt}$ measured at the plagioclase–melt interface decreases progressively with increasing cooling rate according to a logarithmic function described by equation 10 (c). After Mollo *et al.* (2011a). If not observable, error bars are within symbols.

$$\begin{aligned}
 K_{Sr}^{app} = & \frac{1}{2} \left\{ 1 + \operatorname{erf} \left[\sqrt{G^{pl} x / D_{Sr}^{melt}} / 2 \right] \right\} \\
 & + (2K_{Sr}^{true} - 1) \exp \left\{ \left[-K_{Sr}^{true} (1 - K_{Sr}^{true}) (G^{pl} x / D_{Sr}^{melt}) \right] \right. \\
 & \left. \operatorname{erfc} \left[(2K_{Sr}^{true} - 1) / 2 \sqrt{G^{pl} x / D_{Sr}^{melt}} \right] \right\} \quad (9)
 \end{aligned}$$

where K_{Sr}^{true} is the equilibrium partition coefficient expected during equilibrium crystallization, G^{pl} is the crystal growth velocity, D_{Sr}^{melt} is the diffusivity of element i in the melt, and x is the distance the crystal interface moves into the liquid phase and corresponds to the linear dimension of the mineral. Equation 9 is used by Singer *et al.* (1995) to model the effect of rapid crystal growth on the compositional zoning of

natural plagioclase phenocrysts in terms of the dimensionless parameter $G^{pl,x}/D_{Sr}^{melt}$. Figure 12b shows that values ‘modelled’ and ‘measured’ for K_{Sr}^{app} are aligned along two almost identical trends, confirming the disequilibrium growth of plagioclase phenocryst rims due to magma undercooling. There are no experimental data in which the effects of P , T , f_{O_2} and composition are effectively isolated during partitioning of Sr (and other trace elements) between plagioclase and melt at high degrees of undercooling. However, in analogy with the preferential incorporation of Sr in plagioclase, alkali feldspars obtained in the laboratory from a rapidly cooled silicic magma were found to be significantly depleted in Ba leading to lower K_{Ba} with increasing undercooling (Morgan and London, 2003). Besides partition coefficients of Ca and Sr, which are calculated for elements highly compatible with the main solid solution of plagioclase, of particular interest are those of Fe and Mg. These cations occur as minor components in the crystal lattice and, consequently, their partitioning behaviour may potentially reveal the disequilibrium uptake of incompatible elements. If the rate of plagioclase growth is slow enough to ensure that diffusion of elements through the melt maintains near-equilibrium concentrations at the crystal-melt interface, the value of $K_d(Fe-Mg)^{pl-melt}$ is almost constant for a range of isothermal temperatures (Fig. 12c). In contrast, under diffusion-controlled conditions, $K_d(Fe-Mg)^{pl-melt}$ decreases progressively with increasing cooling rate (CR in °C/min) according to the logarithmic function (Mollo *et al.*, 2011a):

$$K_d(Fe-Mg)^{pl-melt} = 2.020 - 0.154(\ln CR + 0.185) \quad (10)$$

Although the fit of the data does not provide a very high correlation coefficient ($R^2 = 0.807$), equation 10 is a first attempt to describe quantitatively the effect of crystallization kinetics on element partitioning. The logarithmic decrease of $K_d(Fe-Mg)^{pl-melt}$ modelled for plagioclase is considerable in comparison with the nominal changes observed during the disequilibrium growth of olivine and clinopyroxene crystals. If chemical species are both highly compatible with the rapidly growing crystals, as in the case of Fe and Mg in olivine (Fig. 10a) and clinopyroxene (Fig. 11a), the achievement of local interface equilibrium between the advancing crystal surface and the diffusive boundary layer does not produce significant changes in the magnitude of the exchange partition coefficient. Conversely, elements incompatible with the crystal lattice can be incorporated into the rapidly growing crystals at non-stoichiometric and non-equilibrium proportions, causing strong deviations from the equilibrium partitioning. The contrasting behaviour observed for the Fe-Mg exchange between plagioclase and mafic minerals reflects the importance of incompatible elements as monitors of magma disequilibrium crystallization and their potential for calibrating new and more powerful tests for equilibrium.

4. Implications of disequilibrium partitioning on modelling magma processes

Igneous thermometers and barometers are important tools for estimating the saturation pressures and temperatures of minerals, as well as for elucidating magma storage

conditions and transport (e.g. Ghiorso and Evans, 2008; Putirka, 2008). Generally, these equations are calibrated using experimental data obtained under equilibrium conditions, and are based on a number of crystal and melt parameters that may influence differently the ability prediction of the models. Other equations are derived using only the crystal components as predictors or, alternatively, the composition of the melt in equilibrium with the mineral of interest. Despite the different model calibrations, igneous thermometers and barometers nearly always assume that the investigated natural compositions approach equilibrium. Eruptive products are commonly associated with magma dynamics in which minerals attempt to re-equilibrate over a range of temperatures and pressures. Moreover, crystals may grow rapidly and incorporate elements from the melt in abundances that do not represent equilibrium partitioning. Given a crystal and melt (host lava or matrix glass) composition, it is not a trivial task to ascertain whether the two are appropriate for use in thermobarometry.

In Fig. 13a clinopyroxene–melt pairs from cooling rate experiments of Mollo *et al.* (2013a) are used as input data for two different barometric equations derived by Putirka (2008). The first barometer is based on both clinopyroxene and melt components. With increasing cooling rate, the error of estimate increases slightly but its value does not exceed the model error of ± 200 MPa. In contrast, the second barometer is primarily dependent on Al_{tot} and calcium-Tschermak components in clinopyroxene. The

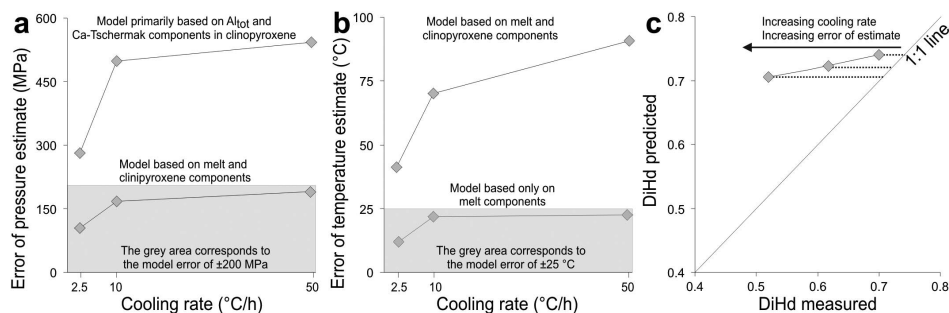


Figure 13. Clinopyroxene–melt pairs from cooling rate experiments of Mollo *et al.* (2013a) are used as input data for two different barometric equations derived by Putirka (2008) (a). The first barometer is based on both clinopyroxene and melt components, yielding a small error of estimate. The second barometer is primarily dependent on Al_{tot} and calcium-Tschermak components in clinopyroxene, yielding a large error of estimate. Cooling rate experiments of Mollo *et al.* (2013a) are also used as input data for two different thermometric equations proposed by Putirka (2008) (b). The thermometer calibrated using only Si, Mg and Ca cation fractions in the melt, is affected by a small error of estimate. In contrast, the thermometer derived using both clinopyroxene and melt components, is affected by a large error of estimate. The equilibrium model proposed by Mollo *et al.* (2013a) is based on the difference between diopside+hedenbergite ($\Delta DiHd$) components predicted for clinopyroxene *via* regression analysis of clinopyroxene–melt pairs in equilibrium conditions, and those measured in the analysed crystals (c). From a theoretical point of view, the equilibrium condition is achieved when the clinopyroxene compositions plot on the one-to-one line of the “DiHd measured” vs. “DiHd predicted” diagram. As the cooling rate increases, the experimental compositions of Mollo *et al.* (2013a) progressively depart from the one-to-one line as a consequence of disequilibrium crystallization conditions.

prediction ability of the model is evidently affected by a systematic error of estimate that substantially increases with increasing cooling rate. As discussed above, the disequilibrium growth of clinopyroxene is controlled by the substitution of $M2(\text{Mg}, \text{Fe}^{2+})$ with $M1(\text{Al}, \text{Fe}^{3+})$ coupled with the substitution of Si for Al in the tetrahedral site to form the Tschermak components. Consequently, the predictive power of the Tschermak-based barometer is remarkably poor, accounting for the kinetically controlled cation redistributions in clinopyroxene. As a further test, the cooling rate experiments of Mollo *et al.* (2013a) are also used as input data for two different thermometric equations proposed by Putirka (2008). Figure 13b shows that the thermometer calibrated using only Si, Mg and Ca cation fractions in the melt yields a relatively small error of estimate, and within the model error of $\pm 25^\circ\text{C}$. This suggests that the error of estimate is minimized when the thermometer reflects the slow-to-intermediate diffusivity of some chemical species in the melt over the timescale of rapid crystal growth. On the other hand, if the thermometer is derived using both clinopyroxene and melt components, its predictive power is more sensitive to disequilibrium growth conditions, and the error of estimate increases systematically with increasing cooling rate. As expected, this is due to the combined effect of the development of a diffusive boundary layer in the melt and the preferential incorporation into the growing crystal of chemical components in non-equilibrium proportions.

Motivated to determine the depth of the magmatic plumbing system beneath a Hawaiian volcano in its post-shield stage of development, Hammer *et al.* (2016) apply clinopyroxene-liquid thermobarometry to an ankaramite from Haleakala, calculating liquids that satisfy Fe-Mg exchange equilibrium by mineral subtraction from the whole rock using mass balance. An earlier application of clinopyroxene thermobarometry to similar rocks from Haleakala (Chatterjee *et al.*, 2005) concluded that polybaric crystallization began 45 km below the volcano's summit, in the mantle. The approach was to assume that growth of Haleakala clinopyroxenes occurs at equilibrium conditions and to transform Na X-ray concentration maps into pressure maps using control points obtained using thermometry (Putirka, 2008). The pressure range corresponding to intracrystalline compositional variation is 60–950 MPa. However, the presence of Na-rich domains associated with euhedral facets in contact with matrix is not consistent with concentric growth at near-equilibrium conditions of decreasing pressure, but rather co-crystallization of both domains under conditions of partial disequilibrium. Analysis of the spatial pattern of element covariation (Welsch *et al.*, 2016) suggests that the crystals are sector zoned, and thus represent kinetic effects associated with rapid growth. Conservatively assuming that low-Na regions are less prone to kinetic partitioning, crystallization pressures for the Haleakala magmas correspond to crustal levels.

Petrologists often use $K_d(\text{Fe}-\text{Mg})^{\text{cpx}-\text{melt}}$ to ascertain whether the clinopyroxene-melt pairs chosen for the estimate of magmatic pressures and temperatures were in equilibrium at the time of crystallization. However, it has long been demonstrated that Fe-Mg exchange has certain limitations and is not a reliable indicator of

clinopyroxene–melt equilibrium for a wide range of compositions (*e.g.* Putirka, 2008). With this in mind, Mollo *et al.* (2013a) performed a new global regression analysis that improves upon one of the most suitable models that test for equilibrium, as presented in Putirka (1999). The equilibrium model is based on the difference between diopside + hedenbergite (ΔDiHd) components predicted for clinopyroxene *via* regression analysis of clinopyroxene–melt pairs in equilibrium conditions, and those measured in the analysed crystals. The value of ΔDiHd provides a more robust test for equilibrium than $K_d(\text{Fe–Mg})^{\text{cpx–melt}}$ due to the fact that deviation from equilibrium occurs in response to the kinetically controlled exchange of equation 3, as diopside and hedenbergite are consumed to form ferrosilite, enstatite, jadeite and Tschermak components. From a theoretical point of view, the equilibrium condition is achieved when the clinopyroxene compositions plot on the one-to-one line of the ‘DiHd measured’ vs. ‘DiHd predicted’ diagram. At this condition, the value of ΔDiHd goes to zero minimizing the error of estimate caused by the accidental use of disequilibrium clinopyroxene–melt pairs as input data for the thermobarometric models (Mollo and Masotta, 2014). Figure 13c shows that, as the cooling rate increases, experimental data from Mollo *et al.* (2013a) progressively depart from the one-to-one line. As a consequence, the value of ΔDiHd increases from 0.05 to 0.19 revealing disequilibrium crystallization conditions that, in turn, cause substantial increase of the error of estimate for pressure (Fig. 13a) and temperature (Fig. 13b).

5. Textural outcomes

5.1. Decompression-driven crystallization in $\text{H}_2\text{O} + \text{CO}_2$ bearing systems

Decompression-driven feldspar crystallization is the focus of several recent experimental studies involving rhyolite and rhyodacite liquid compositions. The studies differ with respect to decompression path type, position of the initial dwell pressure with respect to the equilibrium plagioclase stability curve, the presence or absence of plagioclase crystals in the melt at the start of decompression, and fluid composition. Brugger and Hammer (2010a) examined the control of decompression rate on progressive feldspar crystallization in natural Aniakchak (Alaska) rhyodacite under conditions of H_2O -only fluid saturation (referred to hereafter as ‘ H_2O -saturated’), executing continuous decompression at rates of 10, 2, 1 and 0.5 MPa h^{-1} . Cichy *et al.* (2011) decompressed synthetic rhyodacite in contact with both H_2O -only and $\text{H}_2\text{O}+\text{CO}_2$ fluids starting from below the plagioclase-in curve and proceeding to the quench pressure of 50 MPa at a wide range in rates (72,000, 3,600, 360, 36, 3.6, 1.8 and 0.72 MPa h^{-1}). Using synthetic $\text{CaO–Na}_2\text{O–Al}_2\text{O}_3\text{–SiO}_2$ haplotonalite melt (CNAS rhyolite), Mollard *et al.* (2012) explored the effect of very rapid initial decompression (at rates of 1200, 100 and 30 MPa h^{-1}) on subsequent isobaric crystallization. Martel (2012) studied both isobaric and syn-decompression crystallization of synthetic multicomponent rhyolite relevant to the interstitial liquid in Mt. Pelée (MP) andesite in continuous and multistep experiments performed at 12 decompression rates ranging from 1500 to 0.18 MPa h^{-1} . The experiments included pairs of H_2O -only and $\text{H}_2\text{O}+\text{CO}_2$ fluid-bearing charges; at the initiation of decompression, the former were

crystal-free while the latter contained 3 vol.% plagioclase. Waters *et al.* (2015) prepared initially crystal-free obsidian for relatively slow, continuous decompression (2.9, 1.0, 0.8 and 0.1 MPa h⁻¹) from an initial dwell pressure that was either above or below the plagioclase stability curve at the run temperature. Riker *et al.* (2015) decompressed synthetic rhyodacite relevant to Mount Saint Helens (MSH) interstitial liquid that was in contact with either H₂O-only or H₂O+CO₂ fluid, all containing initial crystals, along disparate paths but with similar total durations.

The decompression paths of these six studies are summarized in plots of log decompression time vs. pressure (Figs 14, 15 and 16), which resemble classical time-

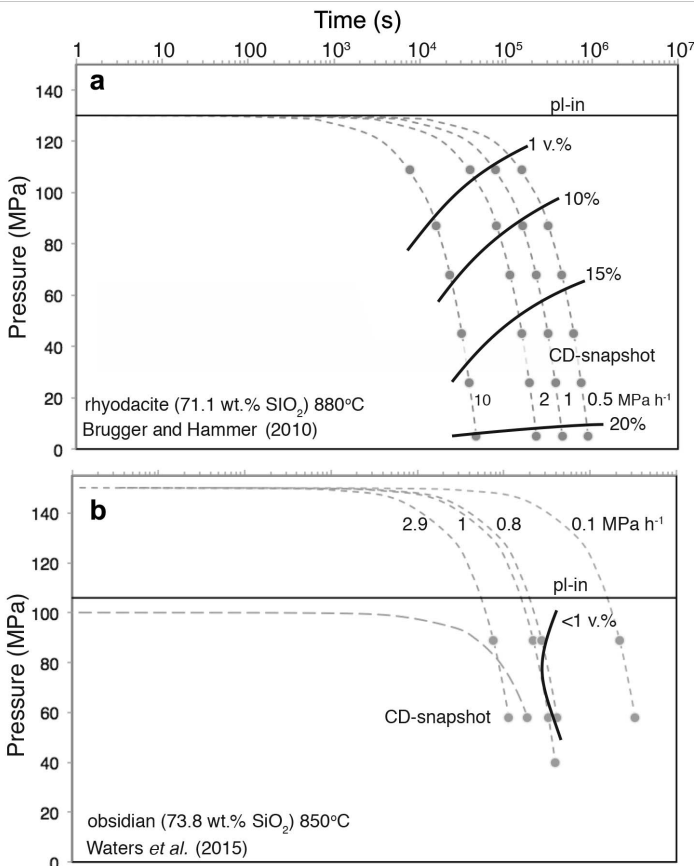


Figure 14. Experimental decompression paths employed by Bruggen and Hammer (2010a) and Waters *et al.* (2015) in panels (a) and (b), respectively. In (b), experiment initiated at 100 MPa (6 MPa below plagioclase-in curve) was performed at the same decompression rate (0.8 MPa h⁻¹) as one of the superliquidus experiments. Although these charges spent the same amount of time below the liquidus these paths do not line up vertically on the plot because the charge that was decompressed from lower initial pressure reached the final pressure sooner.

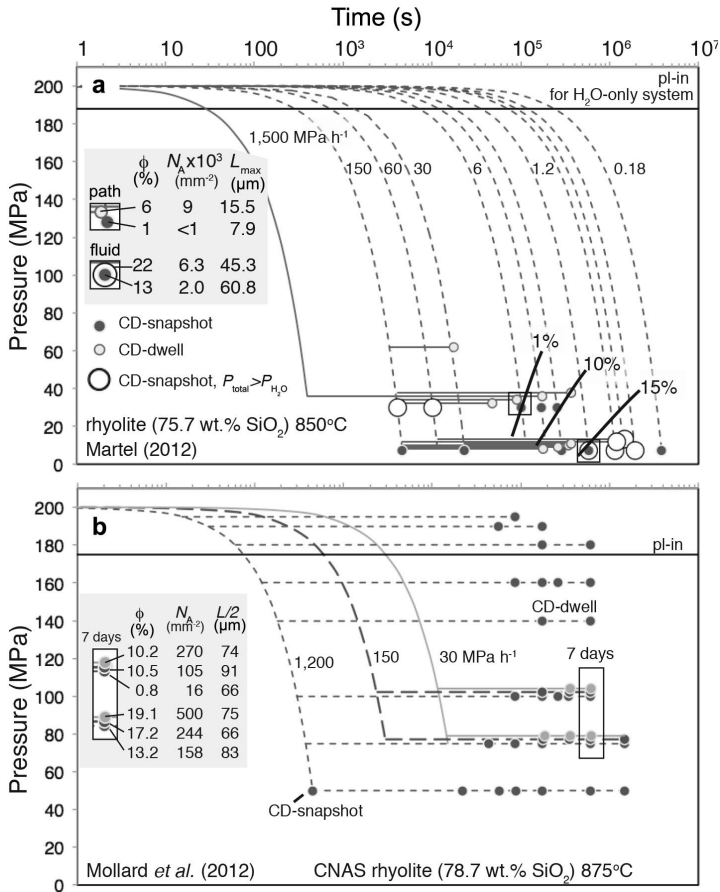


Figure 15. Experimental decompression paths employed by Martel (2012) and Mollard *et al.* (2012) in panels (a) and (b), respectively. Experiments in which cooling occurred in final steps are not shown in panel (a). In (b), the constant volume % plagioclase isograds are drawn using data from CD-snapshot experiments only. Note difference in units of N_A ; feldspar number densities are $\geq 10 \times$ smaller in the experiments of Martel (2012). Crystal lengths are reported by the authors as L_{max} and $L/2$ in the units shown.

temperature-transformation (TTT) diagrams. Constructed from experiments in which temperature is changed nearly instantaneously and then allowed to dwell isothermally, TTT plots allow phase-transformation kinetics to be compared among different materials (*e.g.* Putnis and Bish, 1983; Hammer and Rutherford, 2002; Bowles *et al.*, 2012; Vetere *et al.*, 2013). A similar approach, substituting P_{H_2O} for temperature, was taken in constructing an isobaric crystallization diagram for rhyolite interstitial liquid in natural dacite (Hammer and Rutherford, 2002). Because most of the experiments described here are not isobaric, the plots are not true transformation diagrams, but they do provide a convenient means for comparing experiments that span many orders of

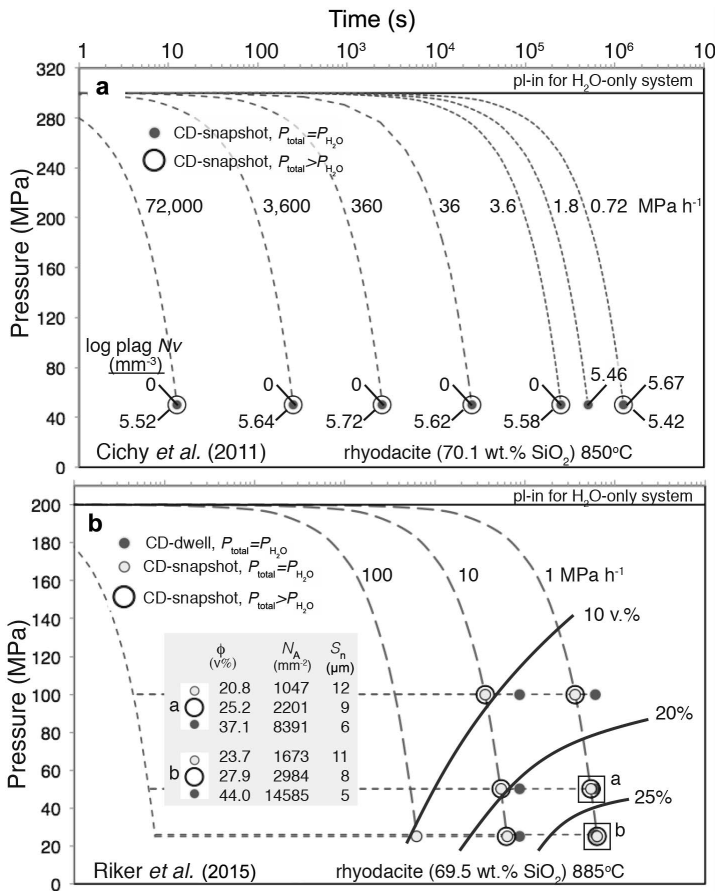


Figure 16. Experimental decompression paths employed by Cichy *et al.* (2011) and Riker *et al.* (2015) in panels (a) and (b), respectively. In (a), the long-dash indicates decompression was conducted continuously. The short dash line pattern indicates multistep decompression (step increment not reported).

magnitude in time scale. Two decompression path types dominate the recent studies. The first type is continuous or quasi-continuous decompression, with single-step decompression (SSD) being the end-member of rapid decompression, followed by a dwell period. This general type is termed CD-dwell, and was utilized by Martel (2012), Mollard *et al.* (2012) and Riker *et al.* (2015). The second type, termed CD-snapshot, is continuous decompression terminated without a final dwell period. The CD-snapshot style was applied by Brugger and Hammer (2010a), Cichy *et al.* (2011), Martel (2012) and Waters *et al.* (2015).

The results from the four studies employing CD-snapshot experiments at H₂O-saturated conditions are contoured for the amount of plagioclase present in run products (Figs 14, 15 and 16), allowing comparison of different materials subjected to similar

decompression path times. The crystallization onset time, related to the glass-forming ability of a material (Vetere *et al.*, 2015), is resolvable from data sets that contain runs without any crystals. For example, crystal-free obsidian decompressed at 850°C from above the plagioclase stability curve (Waters *et al.*, 2015) is more sluggish to begin crystallizing than synthetic rhyolite (Martel, 2012) at the same temperature and decompression rate, as evident from the shorter times represented by the 1 vol.% plagioclase isograds at 30–40 MPa. Continuous decompression at 1 MPa h⁻¹ to 75 MPa produces ~1 vol.% plagioclase in obsidian (Fig. 14b), ~12 vol.% plagioclase in Aniakchak rhyodacite (Fig. 14a), and 20 vol.% in the MSH rhyodacite (Fig. 16b). The more rapid solidification in the latter may be due to decompression from initially higher dissolved H₂O and thus lower melt viscosity. In addition, the obsidian results exhibit a ‘knee’ or minimum in the time at which crystallization begins (over the applied decompression rates) at 75 MPa. Both above and below this pressure, crystallization takes longer to start. In contrast, the natural Aniakchak rhyodacite and synthetic MSH rhyodacite exhibit progressive decrease in the crystallization onset time and monotonic increase in the volume % plagioclase as final pressure decreases. Higher temperature in the latter runs may play some role in this difference, but a more likely pair of related factors is the initial effective superheating and lack of pre-existing crystals in the obsidian experiments. The obsidian data set resembles the “C” shape of transformation curves in which pre-existing growth sites or nuclei are absent; the disappearance or softening of the lower half of the C may be characteristic of systems in which nucleation is not required (*e.g.* Hammer and Rutherford, 2002).

The CD-dwell experiments of Mollard *et al.* (2012) isolate the effect of decompression rate on ensuing crystallization, employing a variety of rates that are so rapid as to preclude syn-decompression crystallization, and then observing the system after dwell times of 2, 4, 7 and 17 days. Melts decompressed at 1200 MPa h⁻¹ have consistently smaller feldspar abundances and smaller crystal-number densities than melts decompressed at 150 or 30 MPa h⁻¹. The results suggest a failure of melt to relax structurally during the decompression (in turn calling into question the Maxwell relaxation time (equation 1) as adequately capturing the ‘structure’ relevant to nucleation), lower rate of crystal nucleation, and insufficient dwell duration for rapidly decompressed materials to respond. This is interesting in the context of paired CD-dwell and CD-snapshot experiments on MP rhyolite (Martel, 2012) and MSH (Riker *et al.*, 2015) rhyodacite in which decompression rate and dwell times are selected to produce similar total time below initial pressure and isolate decompression path as a variable. As was reported for Pinatubo rhyolite interstitial melt (Hammer and Rutherford, 2002), both investigations observe greater crystallinities in the CD-dwell runs than in the rapidly decompressed CD-snapshot runs, and attribute these differences to the higher initial undercooling. Why, if higher initial undercooling stimulates solidification, does the 1200 MPa h⁻¹ decompression not produce greater crystallinity than the 150 or 30 MPa h⁻¹ runs in CNAS rhyolite (Mollard *et al.*, 2012)? Although the decompression rate applied to the MSH rhyodacite (80,000 MPa h⁻¹) was much higher than was applied to CNAS rhyolite (1200 MPa h⁻¹), the MSH rhyodacite

achieved equilibrium feldspar crystallinity after a one-day dwell time at 50 MPa in a nucleation-dominated regime. Evidently, either structural relaxation required for crystal nucleation was faster in the rhyodacite, because of its lower SiO₂ or higher temperature, or the initial superheating of the CNAS rhyolite proved a critical impediment to subsequent crystallization.

5.2. Beyond H₂O and CO₂: Adding other volatiles

Recent experiments broaden the range of fluids in contact with melt during decompression to include species in the H₂O-CO₂-Cl system. Martel (2012) incorporates CO₂ in the MP rhyolite experiments to reduce the amount of dissolved H₂O and drive crystallization during the pre-decompression dwell. By final pressure of 5–10 MPa, charges with pre-decompression crystals have greater crystal-number densities and smaller mean sizes than the initially crystal-free charges, particularly at low decompression rates (Fig. 15a, inset). These features point toward higher rates of nucleation, and thus greater undercooling, in the samples with pre-existing crystals. However, noting the tabular (as opposed to anhedral) morphologies of syn-decompression crystals in the charges containing initial crystals (Martel, 2012) we can infer that the role of the pre-existing crystals is to decrease the degree of undercooling by providing surfaces on which crystallization occurs.

Cichy *et al.* (2011) and Riker *et al.* (2015) modulate the mole fraction of H₂O in the fluid ($X_{\text{H}_2\text{O}}^{\text{fl}}$) from 0.6 to 1.0 and from 0.8 to 1.0 by adding CO₂ in CD-snapshot experiments on Unzen rhyodacite and MSH rhyodacite, respectively (Fig. 16). Both studies also report lower mean feldspar microlite sizes and greater crystal-number densities (with negligible nucleation at the five fastest decompressions in the Unzen experiments and by a factor of 2 in the MSH experiments) in the H₂O-CO₂ runs. The existence of crystals prior to decompression cannot be implicated in these cases, since both capsule preparations (CO₂-free and CO₂-bearing) include pre-existing crystals. Riker *et al.* (2015) attributed the difference to an increase in the temperature of the nucleation rate maximum in the CO₂-bearing material, and yet another factor more likely contributing to the observed textural differences is the effect of lowering dissolved H₂O content, through the addition of CO₂, on the phase relations of the material at the initial dwell conditions. Decreasing dissolved H₂O at constant pressure has the same effect on plagioclase stability as decreasing H₂O during H₂O-saturated decompression: the plagioclase-in temperature increases (Hammer *et al.*, 2002; Médard and Grove, 2008; Fiege *et al.*, 2015). Taking the MP rhyolite as an example, phase equilibrium data under H₂O-saturated conditions (Martel, 2012) indicate that at the plagioclase-in pressure (188 MPa at 850°C), the melt has 5.8 wt.% dissolved H₂O. A reduction to 4.7 wt.% by adding CO₂ has the effect of reducing $P_{\text{H}_2\text{O}}$ to ~132 MPa. In order to equilibrate (achieve zero undercooling) during the initial dwell period, ~5 wt.% plagioclase needs to nucleate and crystallize. Assuming the system does equilibrate, subsequent decompression drives dissolution of this feldspar. By the time the system reaches 132 MPa, the equilibrium system is crystal-free. Thus, decompression from an initially H₂O-undersaturated state is thermally equivalent to

rapidly supercooling, heating to the liquidus, and then cooling the material. Given the influence of fluctuations about the liquidus for the distribution of crystal nuclei (Mills *et al.*, 2011; Mills and Glazner, 2013), it is not surprising that the crystallinity and texture of these final products differ from H₂O-saturated decompression from the liquidus. In addition, the lower dissolved H₂O at all pressures along the decompression path and consequently higher viscosity and instantaneous undercooling are consistent with the higher rate of crystal nucleation in the CO₂-bearing experiments observed by Cichy *et al.* (2011), Martel (2012) and Riker *et al.* (2015).

The presence of crystals at the start of decompression remains an important consideration, related but potentially separable from the degree of melt undercooling. Given the slow rates at which crystals form in evolved liquids, it is possible to initiate an experiment from below the plagioclase-in stability curve and yet have no crystals in the starting material, as is the case in the obsidian decompression experiments (Waters *et al.*, 2015). Future work manipulating initial crystallinity with and without varying the initial dissolved H₂O content will help resolve the contribution of the fluid composition.

The difficulty containing and moderating oxidation in higher-temperature melts within cold-seal pressure vessels suppresses the experimental pursuit of crystallization kinetics studies relative to high silica compositions. Fiege *et al.* (2015) studied crystallization of natural fused trachybasalt from the 2001 eruption of Mt. Etna, applying isothermal continuous decompression rates of 3600, 360 and 36 MPa h⁻¹ from 300 to 70 MPa using a low-flow pressure metering valve for the internally heated pressure vessel (Nowak *et al.*, 2011). In general, a higher rate of decompression results in lower crystallinity (Fig. 17). Replicate decompression histories were applied to fluid-saturated melts coexisting with either H₂O+Cl only, H₂O+Cl+CO₂, and H₂O+Cl+CO₂+S, with the unexpected outcome that the S-bearing samples contain considerably more clinopyroxene (up to 50 vol.%) than the S-free runs (20 vol.%), which match the equilibrium abundances calculated by MELTS thermodynamic simulations (~23 vol.%; Gualda *et al.*, 2012). The run products contain nearly identical dissolved H₂O contents, ruling out a role for H₂O in modulating phase relations. The suggestion by Fiege *et al.* (2015), that a reduction in the activity of H₂O within the fluid phase accounts for the greater clinopyroxene content of the S-bearing system, requires further investigation.

5.3. Cooling-driven crystallization in nominally anhydrous systems

Vetere *et al.* (2015) augment the experimental data set of Vetere *et al.* (2013), which examines the effects of major-element composition, cooling rate, and thermal history on solidification kinetics in oxidized, nominally anhydrous silicate melts (Fig. 18). Together, these studies encompass six cooling rates (1, 7, 620, 3020, 8020 and 9000°C h⁻¹) applied to six glasses homogenized along a mixing line between Icelandic basalt to Aeolian rhyolite from superliquidus conditions. A particular focus is characterizing the glass-forming ability of the materials by determining the minimum cooling rate, or critical cooling rate, R_c , at which <2 vol.% crystallizes. The R_c increases monotonically with increasing basalt component, exhibiting 3.5 orders of magnitude increase between pure

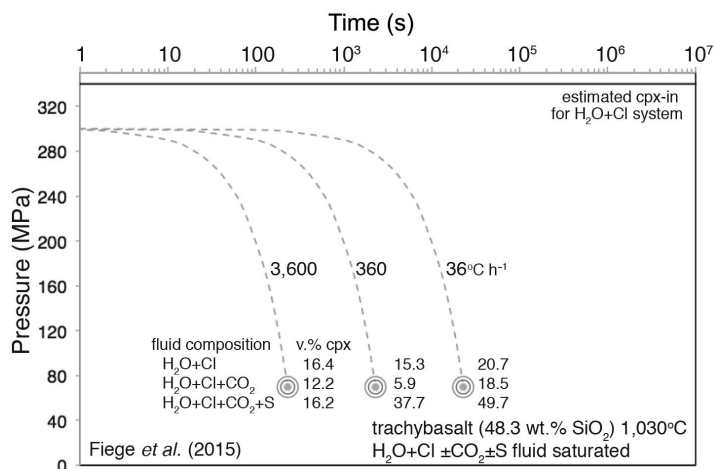


Figure 17. Experimental decompression paths employed by Fiege *et al.* (2015). Plagioclase-in and clinopyroxene-in pressures are not reported, but plotted as 340 MPa because (a) the H₂O+Cl experiment performed at 300 MPa and 1030°C contained 1.5 wt.% clinopyroxene; (b) The experiments with S and CO₂ in the fluid had more crystals (9 wt.% clinopyroxene), and also included spinel; and (c) MELTS indicates 30 wt.% crystals at 1030°C for the H₂O+Cl system. Either the experiments quenched from initial conditions were not equilibrated or MELTS is inaccurate. Either way, the liquidus is probably higher than 300 MPa and the experiments were initiated from below it. Fiege *et al.* (2015) report that the equilibrium clinopyroxene content in the H₂O+Cl system at final pressure of 70 MPa is ~23 wt.%.

rhyolite and the 60–40 wt.% hybrid (Bas₆₀Rhy₄₀) and an additional order of magnitude increase between Bas₆₀Rhy₄₀ and Bas₁₀₀. The results allow Rc (°C h⁻¹) to be expressed as an exponential function of the ratio of non-bridging to tetrahedrally coordinated cations, or NBO/T : (Mysen and Richet, 2005):

$$Rc = 9214 / \{1 + \exp[-[(NBO/T - 0.297)/0.04]]\} \quad (11)$$

Vetere *et al.* (2015) suggested that parameterizations of Rc involving NBO/T may also describe the solidification kinetics of alkalic melts, although Iezzi *et al.* (2008) stressed that small differences in composition produce dramatic differences in Rc in their study of alkali melts. They prepared latite from the Fondo Riccio vent (Campi Flegrei) and trachyte from Agnano Monte Spina using similar procedures to the Vetere *et al.* (2013, 2015) studies. Differences in the SiO₂ (lower by 2.3 wt.% in the latite) and FeO_T (larger by 3.7 wt.%) are probably responsible for the formation of clinopyroxene in the latite at cooling rates of $\leq 30^\circ\text{C h}^{-1}$, echoing an earlier result from cooling experiments on evolved silicic melts (Naney and Swanson, 1980). Interestingly the sub-alkaline andesite from Panarea (Aeolian Islands) studied by Iezzi *et al.*, (2011) begins to crystallize at more rapid cooling rates than the latite or trachyte, but is more sluggish to complete solidification during slow cooling (Fig. 18b). Understanding the structural and compositional controls over the kinetics of crystallization in the last tens of weight% interstitial liquid may require a similarly intense empirical effort.

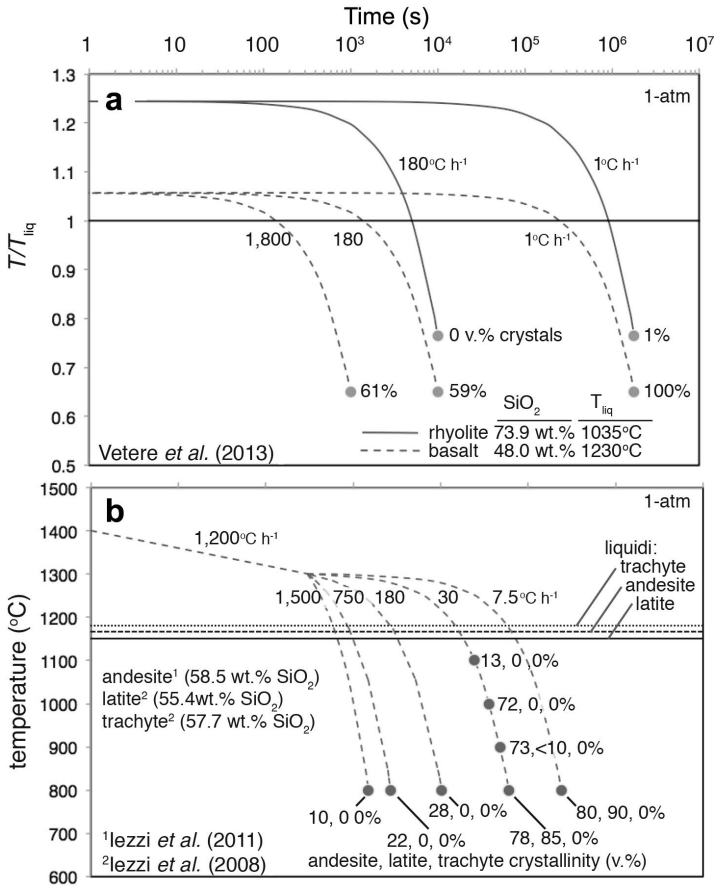


Figure 18. Experimental cooling paths employed by Vetere *et al.* (2013), in panel (a), and Iezzi *et al.* (2008, 2011) in panel (b). In (a), only the two end-member compositions of a suite of six compositions ranging from rhyolite to basalt are included. Temperatures are normalized by the liquidus temperatures in order to compare extents of superheating. The crystallinity for basalt at middle and fastest rates is the average of replicate experiments.

6. Selected applications to volcanological problems

Experimental studies may be designed to resolve a specific petrological or volcanological problem involving the environmental conditions or time scale of a magmatic event. For example, Waters *et al.* (2015) concluded that the melt which ascended to produce crystal-poor rhyolite obsidian must have separated from a multiply-saturated magma at slightly H₂O-undersaturated conditions, as this is the simplest way for the liquid to have been initially superheated in nature. In essence, a constraint from crystal nucleation kinetics is used to address the problem of obsidian petrogenesis. Martel (2012) resolved the magma ascent times associated with plinian

and dome/block and ash flow eruptions of Mt. Pelée to <1 h and 2–5 days, respectively, having characterized the plagioclase textural and compositional characteristics in experiments spanning a wide range in decompression paths. In a similar approach, Andrews and Gardner (2010) study grey and white pumice from the 1,800 ¹⁴C yr BP eruption of Ksudach Volcano, Kamchatka, using H₂O-saturated continuous decompression experiments and find that microlite textures observed in the white pumice require decompression rates of 0.01 MPa s⁻¹, whereas the higher crystallinities and more numerous microlites of grey pumice require decompression at ~0.0025 MPa s⁻¹. Andrews (2014) compares the microlite number densities in dacite from Santa Maria Volcano, Guatemala to decompression-texture relationships from Andrews and Gardner (2010) to constrain magma ascent rate of ~0.005 to 0.01 MPa s⁻¹ during the 1902 Santa Maria eruption. Cichy *et al.* (2011) constrain the ascent rate of 1991–1995 Unzen magma by comparing natural and experimental plagioclase microlite size. The natural glass compositions and microlite lengths are reproduced in H₂O-saturated experiments at decompression rates ≤ 0.0005 MPa s⁻¹ or ~50 m h⁻¹ ascent; decreasing the H₂O activity reduces these rates. The studies described here provide encouraging basis for interpreting natural magmatic storage, ascent, and emplacement processes using experimental calibrations of crystal texture and composition. However, it is important to note the limitations of applicability associated with extrapolation beyond the bulk and phase compositions explicitly represented in an experimental data set, as well as the influence of starting material preparation and other elements of experiment design that influence the final result.

Acknowledgements

This chapter benefited greatly from thoughtful reviews and comments by Laura E. Waters and Harald Behrens. The authors are grateful for the essential editorial guidance of Wilhelm Heinrich and Rainer Abart. J. Hammer acknowledges NSF award EAR-1347887 and the Laboratoire Magmas et Volcans, University of Clermont-Ferrand, France, for support during preparation of this contribution. This is SOEST publication no. 9825.

References

- Albarede, F. and Bottinga, Y. (1972) Kinetic disequilibrium in trace-element partitioning between phenocrysts and host lava. *Geochimica et Cosmochimica Acta*, **36**, 141–156.
- Andrews, B.J. (2014) Magmatic storage conditions, decompression rate, and incipient caldera collapse of the 1902 eruption of Santa Maria Volcano, Guatemala. *Journal of Volcanology and Geothermal Research*, **282**, 103–114.
- Andrews, B.J. and Gardner, J.E. (2010) Effects of caldera collapse on magma decompression rate: An example from the 1800 ¹⁴C yr BP eruption of Ksudach Volcano, Kamchatka, Russia. *Journal of Volcanology and Geothermal Research*, **198**, 205–216.
- Arzilli, F. and Carroll, M.R. (2013) Crystallization kinetics of alkali feldspars in cooling and decompression-induced crystallization experiments in trachytic melt. *Contributions to Mineralogy and Petrology*, **166**, 1011–1027.
- Baker, D.R. (2008) The fidelity of melt inclusions as records of melt composition. *Contributions to Mineralogy and Petrology*, **156**, 377–395.
- Baker, M.B. and Grove, T.L. (1985) Kinetic controls on pyroxene nucleation and metastable liquid lines of descent in a basaltic andesite. *American Mineralogist*, **70**, 279–287.

- Berkebile, C.A. and Dowty, E. (1982) Nucleation in laboratory charges of basaltic composition. *American Mineralogist*, **67**, 886–899.
- Blundy, J.D. and Wood, B.J. (1991) Crystal-chemical controls on the partitioning of Sr and Ba between plagioclase feldspar, silicate melts and hydrothermal solutions. *Geochimica et Cosmochimica Acta*, **55**, 193–209.
- Blundy, J.D. and Wood, B.J. (1994) Prediction of crystal–melt partition coefficients from elastic moduli. *Nature*, **372**, 452–454.
- Blundy, J.D., Robinson, J.A.C. and Wood B.J. (1998) Heavy REE are compatible in clinopyroxene on the spinel ilherzolite solidus. *Earth and Planetary Science Letters*, **160**, 493–504.
- Bowles, J.A., Tatsumi-Petrochilos, L., Hammer, J.E. and Brachfeld, S.A. (2012) Multicomponent cubic oxide exsolution in synthetic basalts: Temperature dependence and implications for magnetic properties. *Journal of Geophysical Research: Solid Earth*, **117**, B03202.
- Brugger, C.R. and Hammer, J.E. (2010a) Crystallization kinetics in continuous decompression experiments: Implications for interpreting natural magma ascent processes. *Journal of Petrology*, **51**, 1941–1965.
- Brugger, C.R. and Hammer, J.E. (2010b) Crystal size distribution analysis of plagioclase in experimentally decompressed hydrous rhyodacite magma. *Earth and Planetary Science Letters*, **300**, 246–254.
- Brugger, C.R. and Hammer, J.E. (2015) Prevalence of growth twins among anhedral plagioclase microlites. *American Mineralogist*, **100**, 385–395.
- Cabane, H., Laporte, D. and Provost, A. (2005) An experimental study of Ostwald ripening of olivine and plagioclase in silicate melts: Implications for the growth and size of crystals in magmas. *Contributions to Mineralogy and Petrology*, **150**, 37–53.
- Chatterjee, N., Bhattacharji, S. and Fein, C. (2005) Depth of alkalic magma reservoirs below Kolekole cinder cone, Southwest rift zone, East Maui, Hawaii. *Journal of Volcanology and Geothermal Research*, **145**, 1–22.
- Cichy, S.B., Botcharnikov, R.E., Holtz, F. and Behrens, H. (2011) Vesiculation and microlite crystallization induced by decompression: a case Study of the 1991–1995 Mt Unzen Eruption (Japan). *Journal of Petrology*, **52**, 1469–1492.
- Coish, R.A. and Taylor, L.A. (1979) The effect of cooling rate on texture and pyroxene chemistry in DSDP Leg 34 basalt: a microprobe study. *Earth and Planetary Science Letters*, **42**, 389–398.
- Conte, A.M., Perinelli, C. and Trigila, R. (2006) Cooling kinetics experiments on different Stromboli lavas: effects on crystal morphologies and phases compositions. *Journal of Volcanology and Geothermal Research*, **155**, 179–200.
- Corrigan, G.M. (1982) Supercooling and crystallization of plagioclase, olivine and clinopyroxene from basaltic magmas. *Mineralogical Magazine*, **46**, 31–42.
- Couch, S., Sparks, R.S.J. and Carroll, M.R. (2003) The kinetics of degassing-induced crystallization at Soufriere Hills volcano, Montserrat. *Journal of Petrology*, **44**, 1477–1502.
- Del Gaudio, P., Mollo, S., Ventura, G., Iezzi, G., Taddeucci, J. and Cavallo, A. (2010) Cooling rate-induced differentiation in anhydrous and hydrous basalts at 500 MPa: implications for the storage and transport of magmas in dikes. *Chemical Geology*, **270**, 164–178.
- DePaolo, D.J. and Getty, S.R. (1996) Models of isotopic exchange in reactive fluid–rock systems: implications for geochronology in metamorphic rock. *Geochimica et Cosmochimica Acta*, **60**, 3933–3947.
- Dingwell, D.B. (1995) Relaxation in silicate melts: Some applications. Pp. 21–66 in: *Structure, Dynamics and Properties of Silicate Melts* (J.F. Stebbins, P. McMillan and D.B. Dingwell, editors). Reviews in Mineralogy, **32**. Mineralogical Society of America, Washington, D.C.
- Dingwell, D.B. and Webb, S.L. (1990) Relaxation in silicate melts. *European Journal of Mineralogy*, **2**, 427–449.
- Dohmen, R. and Blundy, J. (2014) A predictive thermodynamic model for element partitioning between plagioclase and melt as a function of pressure, temperature and composition. *American Journal of Science*, **314**, 1319–1372.
- Dowty, E. (1980) Crystal growth and nucleation theory and the numerical simulation of igneous crystallization. Pp. 419–485 in: *The Physics of Magmatic Processes* (R.B. Hargraves, editor) Princeton University Press, Princeton, New Jersey, USA.
- Falloon, T.J., Danyushevsky, L.V., Ariskin, A., Green, D.H. and Ford, C.E. (2007) The application of olivine geothermometry to infer crystallization temperatures of parental liquids: Implications for the temperatures of MORB magmas. *Chemical Geology*, **241**, 207–233.

- Faure, F., Trolliard, G., Nicollet, C. and Montel, J.M. (2003) A development model of olivine morphology as a function of the cooling rate and the degree of undercooling. *Contributions to Mineralogy and Petrology*, **145**, 251–263.
- Faure, F., Schiano, P., Trolliard, G., Nicollet, C. and Soulestin, B. (2007) Textural evolution of polyhedral olivine experiencing rapid cooling rates. *Contributions to Mineralogy and Petrology*, **153**, 405–416.
- Fiege, A., Vetere, F., Iezzi, G., Simon, A. and Holtz, F. (2015) The roles of decompression rate and volatiles ($\text{H}_2\text{O} + \text{Cl} \pm \text{CO}_2 \pm \text{S}$) on crystallization in (trachy-) basaltic magma. *Chemical Geology*, **411**, 310–322.
- Gamble, R.P. and Taylor, L.A. (1980) Crystal/liquid partitioning in augite: effects of cooling rate. *Earth and Planetary Science Letters*, **47**, 21–33.
- Ghiorso, M.S. and Evans, B.W. (2008) Thermodynamics of rhombohedral oxide solid solutions and a revision of the Fe-Ti two-oxide geothermometer and oxygen-barometer. *American Journal of Science*, **308**, 957–1039.
- Grove, T.L. and Bence, A.E. (1977) Experimental study of pyroxene–liquid interaction in quartz-normative basalt 15597. Pp. 1549–1579 in: *Proceedings of Lunar and Planetary Science Conference, VIII*. Lunar and Planetary Institute, Houston, Texas, USA.
- Grove, T.L. and Raudsepp, M. (1978) Effects of kinetics on the crystallization of quartz-normative basalt 15597: an experimental study. Pp. 585–599 in: *Proceedings of Lunar and Planetary Science Conference, IX*. Lunar and Planetary Institute, Houston, Texas, USA.
- Gualda, G.R., Ghiorso, M.S., Lemons, R.V. and Carley, T.L. (2012) Rhyolite–MELTS: a modified calibration of MELTS optimized for silica-rich, fluid-bearing magmatic systems. *Journal of Petrology*, **53**, 875–890.
- Hammer, J.E. (2006) Influence of f_{O_2} and cooling rate on the kinetics and energetics of Fe-rich basalt crystallization. *Earth and Planetary Science Letters*, **248**, 618–637.
- Hammer, J.E. (2008) Experimental studies of the kinetics and energetics of magma crystallization. Pp. 9–59 in: *Minerals, Inclusions and Volcanic Processes* (K.D. Putirka and F.J. Tepley editors). Reviews in Mineralogy and Geochemistry, **69**. Mineralogical Society of America and Geochemical Society, Washington, D.C.
- Hammer, J.E. (2009) Capturing crystal growth. *Geology*, **37**, 1055–1056.
- Hammer, J.E. and Rutherford, M.J. (2002) An experimental study of the kinetics of decompression-induced crystallization in silicic melt. *Journal of Geophysical Research* **107**.
- Hammer, J.E., Rutherford, M.J. and Hildreth, W. (2002) Magma storage prior to the 1912 eruption at Novarupta, Alaska. *Contributions to Mineralogy and Petrology*, **144**, 144–162.
- Hammer, J.E., Sharp, T.G. and Wessel, P. (2010) Heterogeneous nucleation and epitaxial crystal growth of magmatic minerals. *Geology* **38**, 367–370.
- Hammer, J.E., Jacob, S., Welsch, B., Hellebrand, E. and Sinton, J.M. (2016) Clinopyroxene in postshield Haleakala ankaramite: 1. Efficacy of thermobarometry. *Contributions to Mineralogy and Petrology*, **171**, 7.
- Higgins, M.D. and Roberge, J. (2003) Crystal size distribution of plagioclase and amphibole from Soufriere Hills Volcano, Montserrat: Evidence for dynamic crystallization – textural coarsening cycles. *Journal of Petrology* **44**, 1401–1411.
- Hill, E., Wood, B.J. and Blundy, J.D. (2000) The effect of Ca-Tschermaks component on trace element partitioning between clinopyroxene and silicate melt. *Lithos*, **53**, 203–215.
- Iezzi, G., Mollo, S., Ventura, G., Cavallo, A. and Romano, C. (2008) Experimental solidification of anhydrous latitic and trachytic melts at different cooling rates: The role of nucleation kinetics. *Chemical Geology*, **253**, 91–101.
- Iezzi, G., Mollo, S., Torresi, G., Ventura, G., Cavallo, A. and Scarlato, P. (2011) Experimental solidification of an andesitic melt by cooling. *Chemical Geology*, **283**, 261–273.
- Iezzi, G., Mollo, S., Shahini, E., Cavallo, A. and Scarlato, P. (2014) The cooling kinetics of plagioclase feldspars as revealed by electron-microprobe mapping. *American Mineralogist*, **99**, 898–907.
- Jambon, A., Lussiez, P., Clocchiatti, R., Weisz, J. and Hernandez, J. (1992) Olivine growth rates in a tholeiitic basalt: An experimental study of melt inclusions in plagioclase. *Chemical Geology*, **96**, 277–287.
- Kent, A.J.R., Darr, C., Koleszar, A.M., Salisbury, M.J. and Cooper, K.M. (2010) Preferential eruption of andesitic magmas through recharge filtering. *Nature Geoscience*, **3**, 631–636.
- Kennedy, A.K., Lofgren, G.E. and Wasserburg, G.J. (1993) An experimental study of trace-element partitioning between olivine, orthopyroxene and melt in chondrules – equilibrium values and kinetic effects. *Earth and Planetary Science Letters*, **115**, 177–195.

- Kile, D.E. and Eberl, D.D. (2003) On the origin of size-dependent and size-independent crystal growth: Influence of advection and diffusion. *American Mineralogist*, **88**, 1514–1522.
- Kirkpatrick, R.J. (1981) Kinetics of crystallization of igneous rocks. Pp. 321–397 in: *Kinetics of Geological Processes* (A.C. Lasaga and R.J. Kirkpatrick, editors). Reviews in Mineralogy, **8**, Mineralogical Society of America, Washington, D.C.
- Kirkpatrick, R.J. (1983) Theory of nucleation in silicate melts. *American Mineralogist*, **68**, 66–77.
- Kirkpatrick, R.J., Robinson, G.R. and Hayes, J.F. (1976) Kinetics of crystal growth from silicate melts: anorthite and diopside. *Journal of Geophysical Research*, **81**, 5715–5720.
- Kouchi, A., Sugawara, Y., Kashima, K. and Sunagawa, I. (1983) Laboratory growth of sector zoned clinopyroxenes in the system $\text{CaMgSi}_2\text{O}_6\text{--CaTiAl}_2\text{O}_6$. *Contributions to Mineralogy and Petrology*, **83**, 986–990.
- Kring, D.A. (1985) Use of melt inclusions in determining liquid lines of descent. In *American Geophysical Union, Fall Meeting (San Francisco), Abstracts*, Eos, **66**, 404.
- Kring, D.A. and McKay, G.A. (1984) Chemical gradients in glass adjacent to olivine in experimental charges and Apollo 15 green glass vitrophyres. Pp. 461–462 in: *Proceedings of Lunar and Planetary Science Conference, XV*. Lunar and Planetary Institute, Houston, Texas, USA.
- Kushiro, I. (1974) Melting of hydrous upper mantle and possible generation of andesitic magma: an approach from synthetic systems. *Earth and Planetary Science Letters*, **22**, 294–299.
- Lofgren, G.E. and Smith, D.P. (1980) The experimental determination of cooling rates of rocks: some complications. *Lunar and Planetary Science*, **XI**, 631–633, abstract.
- Lofgren, G.E. and Lanier, A.B. (1992) Dynamic crystallization experiments on the Angra dos Reis achondritic meteorite. *Earth and Planetary Science Letters*, **111**, 455–466.
- Lofgren, G.E., Donaldson, C.H., Williams, R.J., Mullins, O. Jr. and Usselman, T.M. (1974) Experimentally reproduced textures and mineral chemistry of Apollo 15 quartz-normative basalts. Pp. 549–567 in: *Proceedings of Lunar and Planetary Science Conference, V*. Lunar and Planetary Institute, Houston, Texas, USA.
- Lofgren, G.E., Huss, G.R. and Wasserburg, G.J. (2006) An experimental study of trace–element partitioning between Ti–Al–clinopyroxene and melt: Equilibrium and kinetic effects including sector zoning. *American Mineralogist* **91**, 1596–1606.
- Maaløe, S. and Hansen, B. (1982) Olivine phenocrysts of Hawaiian olivine tholeiite and oceanite. *Contributions to Mineralogy and Petrology*, **81**, 203–211.
- Martel, C. (2012) Eruption dynamics inferred from microlite crystallization experiments: Application to Plinian and dome-forming eruptions of Mt. Pelee (Martinique, Lesser Antilles). *Journal of Petrology* **53**, 699–725.
- Martel, C. and Schmidt, B.C. (2003) Decompression experiments as an insight into ascent rates of silicic magmas. *Contributions to Mineralogy and Petrology*, **144**, 397–415.
- Médard, E. and Grove, T.L. (2008) The effect of H_2O on the olivine liquidus of basaltic melts: experiments and thermodynamic models. *Contributions to Mineralogy and Petrology*, **155**, 417–432.
- Mevel, C. and Velde, D. (1976) Clinopyroxenes in Mesozoic pillow lavas from the French Alps: influence of cooling rate on compositional trends. *Earth and Planetary Science Letters*, **32**, 158–164.
- Mills, R.D. and Glazner, A.F. (2013) Experimental study on the effects of temperature cycling on coarsening of plagioclase and olivine in an alkali basalt. *Contributions to Mineralogy and Petrology*, **166**, 97–111.
- Mills, R.D., Ratner, J.J. and Glazner, A.F. (2011) Experimental evidence for crystal coarsening and fabric development during temperature cycling. *Geology* **39**, 1139–1142.
- Mikouchi, T., Miyamoto, M. and McKay, G.A. (1999) The role of undercooling in producing igneous zoning trends in pyroxenes and maskelynites among basaltic martian meteorites. *Earth and Planetary Science Letters*, **173**, 235–256.
- Milman-Barris, M.T., Beckett, J.R., Baker, M.B., Hofmann, A.E., Morgan, Z., Crowley, M.R., Vielzeuf, D. and Stolper, E. (2008) Zoning of phosphorus in igneous olivine. *Contributions to Mineralogy and Petrology*, **155**, 739–765.
- Mollard, E., Martel, C. and Bourdier, J.L. (2012) Decompression-induced crystallization in hydrated silica-rich melts: Empirical models of experimental plagioclase nucleation and growth kinetics. *Journal of Petrology* **53**, 1743–1766.

- Mollo, S. and Masotta, M. (2014) Optimizing pre-eruptive temperature estimates in thermally and chemically zoned magma chambers. *Chemical Geology*, **368**, 97–103.
- Mollo, S., Del Gaudio, P., Ventura, G., Iezzi, G. and Scarlato, P. (2010) Dependence of clinopyroxene composition on cooling rate in basaltic magmas: Implications for thermobarometry. *Lithos*, **118**, 302–312.
- Mollo, S., Putirka, K., Iezzi, G., Del Gaudio, P. and Scarlato, P. (2011a) Plagioclase–melt (dis)equilibrium due to cooling dynamics: implications for thermometry, barometry and hygrometry. *Lithos*, **125**, 221–235.
- Mollo, S., Lanzafame, G., Masotta, M., Iezzi, G., Ferlito, C. and Scarlato, P. (2011b) Cooling history of a dike as revealed by mineral chemistry: A case study from Mt. Etna volcano. *Chemical Geology*, **283**, 261–273.
- Mollo, S., Iezzi, G., Ventura, G., Cavallo, A. and Scarlato, P. (2012a) Heterogeneous nucleation mechanisms and formation of metastable phase assemblages induced by different crystalline seeds in a rapidly cooled andesitic melt. *Journal of Non-Crystalline Solids*, **358**, 1624–1628.
- Mollo, S., Misiti, V., Scarlato, P. and Soligo, M. (2012b) The role of cooling rate in the origin of high temperature phases at the chilled margin of magmatic intrusions. *Chemical Geology*, **322–323**, 28–46.
- Mollo, S., Putirka, K., Misiti, V., Soligo, M. and Scarlato, P. (2013a) A new test for equilibrium based on clinopyroxene–melt pairs: Clues on the solidification temperatures of Etnean alkaline melts at post-eruptive conditions. *Chemical Geology*, **352**, 92–100.
- Mollo, S., Putirka, K., Iezzi, G. and Scarlato, P. (2013b) The control of cooling rate on titanomagnetite composition: Implications for a geospeedometry model applicable to alkaline rocks from Mt. Etna volcano. *Contributions to Mineralogy and Petrology*, **165**, 457–475.
- Mollo, S., Blundy, J., Scarlato, P., Iezzi, G. and Langone, A. (2013c) The partitioning of trace elements between clinopyroxene and trachybasaltic melt during rapid cooling and crystal growth. *Contributions to Mineralogy and Petrology*, **166**, 1633–1654.
- Mollo, S., Giacomoni, P.P., Andronico, D. and Scarlato, P. (2015) Clinopyroxene and titanomagnetite cation redistributions at Mt. Etna volcano (Sicily, Italy): Footprints of the final solidification history of lava fountains and lava flows. *Chemical Geology*, **406**, 45–54.
- Moore, G. and Carmichael, I.S.E. (1998) The hydrous phase equilibria (to 3 kbar) of an andesite and basaltic andesite from western Mexico: Constraints on water content and conditions of phenocryst growth. *Contributions to Mineralogy and Petrology*, **130**, 304–319.
- Morgan, G.B. and London, D. (2003) Trace-element partitioning at conditions far from equilibrium: Ba and Cs distributions between alkali feldspar and undercooled hydrous granitic liquid at 200 MPa. *Contributions to Mineralogy and Petrology*, **144**, 722–738.
- Müller, T., Baumgartner, L.P., Foster, C.T. and Vennemann, T.W. (2004) Metastable prograde mineral reactions in contact aureoles. *Geology*, **32**, 821–824.
- Mullins, W.W. and Sekerka R.F. (1963) Morphological stability of a particle growing by diffusion or heat flow. *Journal of Applied Physics*, **34**, 323–329.
- Muncill, G.E. and Lasaga, A.C. (1987) Crystal-growth kinetics of plagioclase in igneous systems: one atmosphere experiments and approximation of a simplified growth model. *American Mineralogist*, **72**, 299–311.
- Muncill, G.E. and Lasaga, A.C. (1988) Crystal-growth kinetics of plagioclase in igneous systems: isothermal H₂O-saturated experiments and extension of a growth model to complex silicate melts. *American Mineralogist*, **73**, 982–992.
- Mysen, B.O. and Richet, P. (2005) *Silicate Glasses and Melts: Properties and Structure*. Elsevier, Amsterdam.
- Nabelek, P.I. (2007) Fluid evolution and kinetics of metamorphic reactions in calc-silicate contact aureoles – from H₂O to CO₂ and back. *Geology*, **35**, 927–930.
- Naney, M.T. and Swanson, S.E. (1980) The effect of Fe and Mg on crystallization in granitic systems. *American Mineralogist*, **65**, 639–653.
- Nascimento, M.L.F., Ferreira, E.B. and Zannotto, E.D. (2004) Kinetics and mechanisms of crystal growth and diffusion in a glass-forming liquid. *Journal of American Physics*, **121**, 8924–8928.
- Ni, H., Keppler, H., Walte, N., Schiavi, F., Chen, Y., Masotta, M. and Li, Z. (2014) In situ observation of crystal growth in a basalt melt and the development of crystal size distribution in igneous rocks. *Contributions to Mineralogy and Petrology*, **167**, 1003.
- Nowak, M., Cichy, S.B., Botcharnikov, R.E., Walker, N. and Hurkuck, W. (2011) A new type of high-pressure low-flow metering valve for continuous decompression: First experimental results on degassing of

- rhodacitic melts. *American Mineralogist*, **96**, 1373–1380.
- Onuma, N., Higuchi, H., Wakita, H. and Nagasawa, H. (1968) Trace element partitioning between two pyroxenes and the host lava. *Earth and Planetary Science Letters*, **5**, 47–51.
- Pinilla, C., Davis, S.A., Scott, T.B., Allan, N.L. and Blundy, J.D. (2012) Interfacial storage of noble gases and other trace elements in magmatic systems. *Earth and Planetary Science Letters*, **319–320**, 287–294.
- Powell, M.A., Walker, D. and Hays, J.F. (1980) Experimental solidification of a eucrite basalt: microprobe studies. Pp. 896–898 in: *Proceedings of Lunar and Planetary Science Conference, XI*. Lunar and Planetary Institute, Houston, Texas, USA.
- Pupier, E., Duchene, S. and Toplis, M.J. (2008) Experimental quantification of plagioclase crystal size distribution during cooling of a basaltic liquid. *Contributions to Mineralogy and Petrology*, **155**, 555–570.
- Putirka, K.D. (1999) Clinopyroxene + liquid equilibria. *Contributions to Mineralogy and Petrology*, **135**, 151–163.
- Putirka, K.D. (2008) Thermometers and barometers for volcanic systems. Pp. 61–120 in: *Minerals, Inclusions and Volcanic Processes* (K.D. Putirka and F.J. Tepley editors). Reviews in Mineralogy and Geochemistry, **69**. Mineralogical Society of America and Geochemical Society, Washington, D.C.
- Putnis, A. and Bish, D. L. (1983). The mechanism and kinetics of Al, Si ordering in Mg-cordierite. *American Mineralogist* **68**, 60–65.
- Riker, J.M., Cashman, K.V., Rust, A.C. and Blundy, J.D. (2015) Experimental constraints on plagioclase crystallization during H₂O- and H₂O-CO₂-saturated magma decompression. *Journal of Petrology*, **56**, 1967–1998.
- Roeder, P.L. and Emslie, R.F. (1970) Olivine–liquid equilibrium. *Contributions to Mineralogy and Petrology*, **29**, 275–289.
- Roselle, G.T., Baumgartner, L.P. and Chapman, J.A. (1997) Nucleation-dominated crystallization of forsterite in the Ubehebe peak contact aureole, California. *Geology*, **25**, 823–826.
- Sato, H. (1995) Textural difference of pahoehoe and aa lava of Izu–Oshima volcano, Japan – an experimental study on population density of plagioclase. *Journal of Volcanology and Geothermal Research*, **66**, 101–113.
- Scarlato, P., Mollo, S., Blundy, J., Iezzi, G. and Tiepolo, M. (2014) The role of natural solidification paths on REE partitioning between clinopyroxene and melt. *Bulletin of Volcanology*, **76**, 810.
- Schiavi, F., Walte, N. and Keppler, H. (2009) First in situ observation of crystallization processes in a basaltic–andesitic melt with the moissanite cell. *Geology*, **37**, 963–966.
- Schnare, D.W., Day, J.M.D., Norman, M.D., Liu, Y. and Taylor L.A. (2008) A laser–ablation ICP–MS study of Apollo 15 low-titanium olivine-normative and quartz-normative mare basalts. *Geochimica et Cosmochimica Acta*, **72**, 2556–2572.
- Shea, T. and Hammer, J.E. (2013) Kinetics of cooling- and decompression-induced crystallization in hydrous mafic–intermediate magmas. *Journal of Volcanology and Geothermal Research*, **260**, 127–145.
- Shimizu, N. (1981) Trace element incorporation into growing augite phenocryst. *Nature*, **289(5798)**, 575–577.
- Singer, B.S., Dungan, M.A. and Layne, G.D. (1995) Textures and Sr, Ba, Mg, Fe, K and Ti compositional profiles in volcanic plagioclase: clues to the dynamics of calcalkaline magma chambers. *American Mineralogist*, **80**, 776–798.
- Smith, R.K. and Lofgren, G.E. (1983) An analytical and experimental study of zoning in plagioclase. *Lithos*, **16**, 153–168.
- Smith, V.G., Tiller, W.A. and Rutter, J.W. (1955) A mathematical analysis of solute redistribution during solidification. *Canadian Journal of Physics*, **33**, 723–745.
- Swanson, S.E. (1977) Relation of nucleation and crystal-growth rate to the development of granitic textures. *American Mineralogist*, **62**, 966–978.
- Tammann, G. and Mehl, R.F. (1925) *The States of Aggregation*. Van Nostrand Reinhold, New York.
- Thornber, C.R. and Huebner, J.S. (1985) Dissolution of olivine in basaltic liquids: experimental observations and applications. *American Mineralogist*, **70**, 934–945.
- Tsuchiyama, A. (1985) Crystallization kinetics in the system CaMgSi₂O₆–CaAl₂Si₂O₈: development of zoning and kinetics effects on element partitioning. *American Mineralogist*, **70**, 474–486.
- Ujike, O. (1982) Microprobe mineralogy of plagioclase, clinopyroxene and amphibole as records of cooling rate in the Shirotori–Hiketa dike swarm, northeastern Shikoku, Japan. *Lithos*, **15**, 281–293.

- Vetere, F., Iezzi, G., Behrens, H., Cavallo, A., Misiti, V., Dietrich, M., Knipping, J., Ventura, G. and Mollo, S. (2013) Intrinsic solidification behaviour of basaltic to rhyolitic melts: A cooling rate experimental study. *Chemical Geology*, **354**, 233–242.
- Vetere, F., Iezzi, G., Behrens, H., Holtz, F., Ventura, G., Misiti, V., Cavallo, A., Mollo, S. and Dietrich, M. (2015) Glass forming ability and crystallisation behaviour of sub-alkaline silicate melts. *Earth Science Reviews*, **150**, 25–44.
- Walker, D., Kirkpatrick, R.J., Longhi, J. and Hays, J.F. (1976) Crystallization history of lunar picritic basalt samples 12002: phase equilibria and cooling rate studies. *Geological Society of America Bulletin*, **87**, 646–656.
- Waters, L.E., Andrews, B.J. and Lange, R.A. (2015) Rapid crystallization of plagioclase phenocrysts in silicic melts during fluid-saturated ascent: Phase equilibrium and decompression experiments. *Journal of Petrology*, **56**, 981–1006.
- Watson, E.B. and Liang, Y. (1995) A simple model for sector zoning in slowly grown crystals: implications for growth rate and lattice diffusion, with emphasis on accessory minerals in crustal rocks. *American Mineralogist*, **80**, 1179–1187.
- Watson, E.B. and Müller, T. (2009) Non-equilibrium isotopic and elemental fractionation during diffusion-controlled crystal growth under static and dynamic conditions. *Chemical Geology*, **267**, 111–124.
- Welsch, B., Faure, F., Famin, V., Baronnet, A. and Bachelery, P. (2013) Dendritic crystallization: A single process for all the textures of olivine in basalts? *Journal of Petrology*, **54**, 539–574.
- Welsch, B., Hammer, J.E. and Hellebrand, E. (2014) Phosphorus zoning reveals dendritic architecture of olivine. *Geology*, **42**, 867–870.
- Welsch, B., Hammer, J.E., Baronnet, A., Jacob, S., Hellebrand, E. and Sinton, J.M. (2016) Clinopyroxene in postshield Haleakala ankaramite 2. Texture, compositional zoning, and supersaturation in the magma. *Contributions to Mineralogy and Petrology*, **171**, 6.
- Wood, B.J. and Blundy, J.D. (1997) A predictive model for rare earth element partitioning between clinopyroxene and anhydrous silicate melt. *Contributions to Mineralogy and Petrology*, **129**, 166–181.
- Wood, B.J. and Blundy, J.D. (2001) The effect of cation charge on crystal–melt partitioning of trace elements. *Earth and Planetary Science Letters*, **188**, 59–72.
- Wood, B.J. and Trigila, R. (2001) Experimental determination of aluminium clinopyroxene–melt partition coefficients for potassic liquids, with application to the evolution of the Roman province potassic magmas. *Chemical Geology*, **172**, 213–222.
- Zhang, Y. (2010) Diffusion in minerals and melts: theoretical background. Pp. 5–60 in: *Diffusion in Minerals and Melts* (Y. Zhang and D. Cherniak, editors). Reviews in Mineralogy and Geochemistry, **72**. Mineralogical Society of America and Geochemical Society, Washington, D.C.
- Zhou, W., Van der Voo, R., Peacor, D.R. and Zhang, Y. (2000) Variable Ti content and grain size of titanomagnetite as a function of cooling rate in very young MORB. *Earth and Planetary Science Letters*, **179**, 9–20.